AST5-CT-2006-030729

ATLLAS

Aerodynamic and Thermal Load Interactions with Lightweight Advanced Materials for High Speed Flight

SPECIFIC TARGETED RESEARCH PROJECT

Thematic Priority – 1.4
AERONAUTIC and SPACE

Final Public Report:
Objectives and Achievements for the ATLLAS Project

Start date of project: 1st of October 2006

Duration: 39 months

Project coordinator: Dr J. Steelant

Project Coordinator Organisation name: ESA-ESTEC

Project co-funded by the European Commission within the Sixth Framework Programme		
Dissemination Level		
PU	Public	X
PP	Restricted to other programme participants (including the Commission Services)	
RE	Restricted to a group specified by the consortium (including the Commission Services)	
CO	Confidential, only for members of the consortium (including the Commission Services)	

APPROVAL

Title	**issue**	revision
Final Activity Report	2	0

Author(s)	**date**
J. Steelant (ESA-ESTEC)	20/11/2010
J. Longo (DLR)	20/11/2010
M. Kuhn (DLR)	20/11/2010
S. Soller (ASTRIUM)	20/11/2010
M. Bouchez (MBDA)	20/11/2010

Approved by	**Date**
J. Steelant (ESA-ESTEC)	25/11/2010

Table of Contents Page

1. Executive summary 7
2. Introduction 10
3. Project Objectives 11
4. Novel Concepts for High-Speed Flights 13
5. Lightweight Airframe Materials for Sustained High-Speed Flight 24
6. Increased Engine Thermal Efficiency: Novel Cooling Concepts 29
7. Material-Aero-Thermal Interaction Modelling 45
8. Conclusions 54
References 55

List of Figures

Figure 1: Mach 3 vehicle CAD-model (left); configuration with fuselage and wing skins off (right). Cyan: air flow path; blue: wing nozzle and thrust surfaces; red: fuel tanks; magenta: cabin… 13

Figure 2: Mach 3.5 configuration: Mach distribution including exhaust expansion in the aft part of the wing: top: M=0.4, Alpha=0; bottom: M=3.5, Alpha=0. 14

Figure 3: M3T engine flow schematic 14

Figure 4: FEM Materials group. 15

Figure 5: MDO current results: top: initial configuration, bottom: current configuration. 16

Figure 6: Stress-levels (von Mises) for a tail load case. 17

Figure 7: Sensitivity to forebody and ramp deformations for the Mach 6 configuration. 17

Figure 8: Stress-levels for a temperature-case of ΔT = 500°C. 18

Figure 9: Automatic multi-lobe tank generation with aircraft fuselage constraint. 18

Figure 10: Measured (solid) and MOC (dashed) signatures for the SSBD (blue) and F-5E (red), assuming a ground reflection factor of 1.8 19

Figure 11: Ground sonic boom of ATLLAS Mach 6 configuration. Histograms for peak overpressure (in red – in Pa) and rise time (in blue – in ms) for Edwards (left column) and Le Havre (right column) for West (top line) and East (bottom line) heading. 20

Figure 12: Comparison of produced lift and required power for energy deposition and mechanical deflection. 21

Figure 13: Mach 3 vehicle cabin cross section and proposed wall make-up. Fuselage outer skin and structural zone (red), inner insulation zone, air gap, for cabin return air and inner skin. .. 21

Figure 14: Cruise efficiency in function of flight Mach number for existing subsonic and supersonic vehicles along with the ATLLAS M3T (new concept) and the ATLLAS M6 (Optimized by means of MDO from the existing Hycat configuration of Lockheed). 22

Figure 15: Indicative specific fuel consumption values for various sub- and supersonic aircraft in function of Mach number. 23

Figure 16: Radiation equilibrium wall temperature at stagnation point, Mach 6, ε = 0.85, Λ = 65°. 24

Figure 17: Sandwich panels with a HSP core for structural testing and its mechanical modelling for its compressive behaviour. Left: 6x6x2 hollow spheres with t=0.56mm; right: 4x4x6 hollow spheres with t=0.56mm 25

Figure 18: UHTC air intake prototype (40x40x1.9mm3); arc jet sample Ø 26,5; thermal and chemical tests at the L2K facility of DLR. 26

Figure 19: Specific strength vs. temperature 27

Figure 20: C/C-SiC leading edge with radius 2 mm (left) and sharp-edged (right) 28

Figure 21: Leading edge model and its mesh for numerical simulation at FOI 28

Figure 22: Simulated pressure contour along the symmetry plane (left picture) and simulated wing temperature distribution for OXIPOL (in Kelvin) at α = 5°and δ = 0° (right picture). 28

Figure 23: DLR Cologne heat flux sensor: ANSYS model, first probe and temperature sensor response 30

Figure 24: Design of reference heat flux sensor (left) and L3K windtunnel test results with 3000kW/m2 heat flux load 30

Figure 25: Single-element combustion chamber designed and characterized for ATLLAS 31

Figure 26: Film applicator details (sketch and 3D cut-away) 31

Figure 27: Heat Flux Density over Axial Position (Mean with RMS) 32

Figure 28: WHIPOX liners manufactured by DLR for transpiration cooling tests at TUM, from left to right: WHIPOX, C/C, WHIPOX, OXIPOL 32

Figure 29: Measured pressure drops of CMC samples before, in-between and after hot run tests 33

Figure 30: OXIPOL, sample (left) and CT section definitions at dedicated (a) circumferential (as seen from front face to exit) and (b) axial positions 33

Figure 31: PSR-CMC segment manufacturing process: CT scan after R.CVI process 34

Figure 32: PSR-CMC liner machined for joining with the microfibre shells 34

Figure 33: Experimental setup for convectively cooled CMC's at TUM (left), specimen after end of GN2 cooling test campaign (right) 35

Figure 34: Heat fluxes recorded with nitrogen cooling (left) and kerosene cooling (right) 35

Figure 35: Cross sectional view of Ox-rich combustor (circles indicate location of hot gas temperature measurements) 36

Figure 36: Ox-rich combustor setup 36

Figure 37: Hardware samples after test 37

Figure 38: Haynes 230 composition: XPS depth profile at stagnation point after combustion 37

Figure 43: Pressure Drop vs. Through-Flow velocity in hot-gas tests: Comparison of Experimental Results with analytical model. Left: random C/C PH1732-08 L=5 mm. Right: random C/C PH1732-03 L=10 mm. 40

Figure 45: Cooing Efficiency of Carbotex^{SI} CT in cross-flow configuration 41

Figure 46: Surface Temperature Distribution of the Effusion Cooled Multi-Perforated Plate at M = 2:1 and Tt;g = 500 K (flow from left to right) 42

Figure 47: Cooling Efficiency of the Multiperforated Plate (MPP) 42

Figure 48: Relative comparison of cooling efficiencies for effusion, transpiration and convective cooling 43

Figure 49: Baseline EINOx development equivalence ratio ∅ =0.42H2 combustion for Mach 6 vehicle 43

Figure 50: Investigation of coupled phenomena on Mach 6 generic aircraft 45

Figure 51: NS computations of TUM experiment (left: 3D MBDA with CFDACE; right: 2D ASTRIUM with ROCFLAM) 46

Figure 52: Basic test case of heat transfer in porous media from Marseille laboratory (Rahli et alii) 46

Figure 53: Comparison between experimental and numerical results: temperature at the interface for different blowing ratios and core flow total temperatures: left: $T_{t,g}$ = 450 K; right $T_{t,g}$ = 1060 K. 47

Figure 54: Numerical and experimental cooling efficiency vs. blowing ratio for $T_{t,g}$ = 450 K, 600K and 1060 K. 47

Figure 55: Helium coolant injection: density contours. 48

Figure 56: Cooling efficiency as a function of coolant mass flow and coolant mass flowC_p/ C_p(Air).for Air, Helium and Hydrogen.* 48

Figure 57: Ignition location as a function of increasing blowing ratio: from top to the bottom, case 1 to case 6. 49

Figure 58: Combustion ignition location related to reflected shock wave: case 6 (density contours). 49

Figure 59: Normalized Skin friction 50

Figure 60: Hot and cold temperature maps of the metallic multi-perforated plate in ITLR hot flow conditions..... 50

Figure 61: Aerothermal loading of a nozzle sandwich panel with a Ti-sheet on the cold side and C/C-SiC on the hot side 51

Figure 62: Typical breakdown process within a compressible laminar boundary layer downstream of roughness. 52

Figure 63 : Effect of roughness on transition: ATLLAS experimental and numerical results compared with a proposed transition criterion compared to other available criteria. 52

Figure 64: Hot film gauged model with instrumentation detail (left) and thermocouple equipped flat plate in front of the HEAT Mach 6 nozzle (right) 53

1. Executive summary

The project ATLLAS (Aerodynamic and Thermal Load Interactions with Lightweight Advanced Materials for High Speed Flight) kicked off in October 2006 and ended in December 2009. Its main objective was to evaluate and assess potential high-temperature resistant materials for sustained super- and hypersonic flight. This covers both materials for the external geometry as well as for the internal combustor geometries. The project, led by ESA-ESTEC, was co-funded by the European Commission under the 6th Framework Program and involved a consortium of 13 partners from industry, research institutions and universities.

The objective was to identify and assess lightweight advanced materials and structures along with more general technologies, including simulation tools, enabling to withstand ultra high temperatures and heat fluxes encountered during high-speed flight above Mach 3. At these high speeds, classical materials used for airframes and propulsion units are not longer feasible and need to be replaced by high-temperature, lightweight materials, with active cooling of some parts.

First, the overall design for high-speed transport vehicles was revisited to explore potential increase in lift/drag ratio and volumetric efficiency through the 'compression lift' and 'waverider' principles, taking into account sonic boom reduction.
Second, materials and cooling techniques and their interaction with the aero-thermal loads were addressed for both the airframe and propulsion components. The former focused on sharp leading edges, intakes and skin materials coping with different aerothermal loads, the latter on combustion chamber liners. After material characterisation and shape definition at specific aero-thermal loadings, dedicated on-ground experiments were conducted. Both Ceramic Matrix Composites (CMC) and heat resistant metals were tested to evaluate their thermal and oxidiser resistance. In parallel novel cooling techniques based on transpiration and electro-aerodynamics principles were investigated.
Combined aero-thermal experiments tested various materials specimens with a realistic shape such as sharp leading edges at extreme aero-thermal conditions for elevated flight Mach numbers. Dedicated combustion experiments on CMC combustion chambers allowed the reduction of combustion liner cooling and an overall thermal efficiency increase. The effect of NOx-production was assessed for these high-speed engines.
Finally, particular aero-thermal-material interactions strongly influence the aerothermal loadings. Conjugate heat transfer, transpiration cooling and compressible transition phenomena were investigated and modelled.

ATLLAS was carried out in 39 months by a 13-member consortium. As major European manufacturers in the highly competitive high-tech field of aeronautical high-speed flight design and manufacturing, ASTRIUM (D), MBDA (F) and EADS-Innovation Works (D) provided the technical needs and application-specific expertise. One SME industrial partner, GDL (UK), has developed a design method particularly suited to highly integrated engine/airframes and applied the method to the Mach 3 aircraft design. Another SME, ALTA (I), has developed renowned skills and expertise the field of high-speed experiments. The groups belonging to research centres, ESTEC (NL), DLR (D), ONERA (F), FOI (S), and universities, Stuttgart (D), Munich (D), Southampton (UK) and UPMC at Paris (F), are all working for long-time on specific issues of propulsion, combustion and aerodynamics with close contact to industry in bilateral, national and international collaborations. They provided basic knowledge, investigation means and testing facilities.

Consortium partners:

Partic. no.	Participant name	Participant short name	Country
1	European Space Agency – European Space Research and Technology Centre	ESA-ESTEC	NL
2	European Aeronautic Defence and Space	EADS	D
3	MBDA-France	MBDA	F
4	Alta S.p.A.	ALTA	I
5	Deutsches Zentrum für Luft- und Raumfahrt	DLR	D
6	Office National d'Etudes et de Recherches Aérospatiales	ONERA	F
7	Totalförsvarets Forskningsinstitut	FOI	S
8	Gas-Dynamics Limited	GDL	UK
9	University of Southampton	SOTON	UK
10	University of Stuttgart	ITLR	D
11	University of Munich	TUM	D
12	EADS Corporate Research Centre	CRC	D
13	Université Pierre et Marie Curie	UPMC	Fr

Nomenclature

C/C	Carbon fibre reinforced carbon CMC
C/C-SiC	Carbon fibre reinforced silicon carbon CMC
CFD	Computational Fluid Dynamics
CMC	Ceramic Matrix Composites
CT	Computer Tomography
DNS	Direct Numerical Simulation
EDX	Energy Dispersive X-Ray
EHD	Electro Hydro Dynamics
ESCA	Electron Spectroscopy for Chemical Analysis
FEM	Finite Element Method
GOX	Gaseous Oxygen
L/D	Lift/drag ratio (important parameter for aircraft range)
LPI	Liquid Polymer Infiltration
LSI	Liquid Silicon Infiltration
MDO	Multi-Disciplinary Optimization
MHD	Magneto Hydro Dynamics
NDI	Non Destructive Investigation
OXIPOL	OXIde based CMC based on POLymers
PTAH	Paroi Tissée Application Hypersonique
RANS	Reynolds-Averaged Navier-Stokes Equations
RBCC	Rocket-Based Combined Cycle
RTM	Resin Transfer Moulding
SEM	Scanning Electron Microscope
SOCAR	Simple Operational Composite for Advanced Ramjet
SST	SuperSonic Transport
STREP	Specific Targeted Research Project
TBCC	Turbine Based Combined Cycle
TN	Technical Note
UHTC	Ultra High Temperature Composites
Whipox	Wound Highly Porous Oxide CMC
WP	Workpackage

2. Introduction

For high-speed aircraft, material and cooling issues for both airframe and engine are one of the key elements which force the designer to limit the flight Mach number. The expected benefits of economical, high-performance and high-speed civil-aircraft designs that are being considered for the future will be realized only through the development of light-weight, high-temperature composite materials for structure and engine applications enabling reduction of weight, fuel consumption, and direct operating costs [2].
When aircraft fly at high speed for long periods of time, friction from the air passing over the aircraft heats up the outer surfaces of the fuselage and wings. For example, an aircraft flying at Mach 3 experiences a temperature increase of ~330K from this kinetic heating. The maximum temperature of the outer surface would be at 620K. For Mach 6 the outer surface would be ~1500K. The extremely severe combination of component stress levels and high temperature operating conditions, as well as the requirement for an extended 25,000-cycle service-life, introduce the challenge of utilizing advanced materials without incurring excessive weight and cost penalties. Such materials' behaviour and related manufacturing processes are beyond current commercial experience and only little information is available.

Propulsion engineers are mainly confronted with increasing difficulties arising from high engine temperatures. The structural total-life requirements for the SST propulsion system are the same 30,000 hours as in subsonic commercial engines [3]. Nevertheless, subsonic aircraft engines spend less than 10% of their mission time at the most severe engine conditions. On the contrary, SST engines spend about 60% of the mission time under the most severe combination of component stress levels and high temperature conditions. The aim is to utilize advanced materials to cope with the high temperatures without introducing excessive weight and cost penalties.

Moreover, the engine designer faces additional problems because of the higher operating temperatures required to produce the higher thrust. At Mach 2 air enters the intake at about 210K, is compressed in the intake to about 400K at the face of the engine and leaves the high-pressure compressor at 820K. At Mach 3 this rises exponentially to respectively 600K and 1250K.

Viable combustors concepts, having a long life goal of 18,000 hours, depend on the development and demonstration of a new class of high temperature ceramic matrix composites (CMC) for which no previous commercial practice exists [4]. At the same time, lightweight, high strength and high stiffness metallic, intermetallic and ceramic composite materials are being examined for the exhaust nozzle design in order to meet engine noise and weight requirements [5][6].

The major challenge arises from the total airframe configuration. To meet it the aerodynamicist has to produce a satisfactory compromise between two inherently conflicting requirements: the need for minimum drag in supersonic flight and the need for controllability and ease of handling in subsonic flight. From a design point of view, the lift-to-drag (L/D) ratio is the most important aerodynamic parameter of airliners, affecting essential economic-related performance such as maximum range, payload and fuel consumption. The primary cause of SSTs' high specific fuel consumption (SFC) is the dramatic fall in airplane's L/D ratio at supersonic speeds. Concorde, for example, experiences an L/D reduction in the order of one-half that of subsonic jets.

The main goal, therefore, is to increase the lift-to-drag ratio throughout the speed regime of the next generation SST. Methods needs to be evaluated which include optimisation schemes coupled with state-of-the-art computational fluid dynamic (CFD) solvers, as well as non-linear design methods. The development and application of Multi-Disciplinary Optimisation tools involving aerodynamics, propulsion, structure and flight mechanism are in the end required to realize an optimum integrated airframe/propulsion aircraft. It is however not the intent to evaluate new and advanced propulsion concepts as this is investigated within the EC-project LAPCAT [1]. Here we start from existing engines (turbojets) or engines which are within technical range (turbo-ramjets). Finally, a SST design should also consider the impact of the sonic boom impact and assess the NOx emissions along with possible measures to reduce it [7][8].

3. Project Objectives

The ATLLAS project aims at providing a sound technological basis for the industrial introduction of lightweight advanced high-speed aircrafts for the second half of this century, defining the most critical RTD-building blocks to achieve this goal and finally to investigate in depth these critical technologies by developing and/or applying dedicated analytical, numerical and experimental tools.

Two supersonic aircrafts concepts are evaluated. The primary cause of the high specific fuel consumption for high-speed transportation is the dramatic fall in lift/drag ratio at supersonic speeds. The main goal is to find out if the established empirical L/D barrier is fundamental or if it can be broken by careful design and in particular by close integration of the airframe and the engine. The study investigates an aircraft configuration suited to Mach 3 flight and another for Mach 6. Areas of critical aero-thermal loads are identified and evaluated.

Critical technologies for both the external airframe and the propulsion units are assessed. The major issues addressed are sonic boom and heat transfer reduction, high temperature resistant materials which should be both lightweight and long-duration oxidation-resistant, novel cooling techniques, particular aerodynamic phenomena related to compressibility, and fuels that have both high energy content and good heat sink capability.

The concept of boom minimization is based on suppressing the coalescence of multiple secondary shock waves caused by the SST in supersonic flight, so that the overpressure (DP) at ground level is reduced. This can be achieved through the manipulation of aircraft's design characteristics, resulting in an optimised N-wave pressure signature with significant sonic boom loudness attenuation. In the proposed program eliminating the fuselage bow shock and the rear reattachment shock is investigated by careful integration with the propulsion system. Alternatively, creation of cold plasma in front of nose or leading edges allows the change of shock structure and its related strength.

Specific objectives for the envisaged concepts are related to materials and cooling. Lightweight airframe components are clearly needed for both concepts. The multi-functionality of hollow-sphere structures for aeronautical applications is evaluated for their low-density, thermal protection, acoustic absorption. Also Ultra-High Temperature Composites and oxidation resistant CMC materials for sharp leading edges and air intakes at sustained high heat fluxes typical for high-speed transport are investigated allowing the generation of a database for possible concepts and materials.

Also lightweight engine components are needed allowing the increase of the combustion liner and turbine vanes temperature resulting into lower NOx-emission and higher turbine inlet temperatures leading towards higher thermal and propulsion efficiency. Long-term oxidation and wear resistance of the combustion liner for lean combustion conditions are performed for the same reasons of setting up a database for possible concepts materials.

Despite the use of high-temperature protection systems, the imposed heat fluxes for airframe and engine still require the use of direct or indirect cooling to control material temperature. The initiation of high-temperature resistant materials automatically requires the (re)-investigation of novel cooling concepts by evaluation of various types of cooling processes (film, transpiration, effusion) within propulsion units with respect to cycle efficiency and controlling operational material temperatures. Also EHD cooling principles by altering the shock position and strength and hence the related stagnation heat flux are studied.

The emphasis in the area of loads definition is to develop and verify models to predict the combined effect of aero-thermal and material interaction on several lightweight high-temperature resistant materials. This is accomplished by integrating existing aerodynamic, heat-transfer, and structural codes. The results are then calibrated and verified with simplified experiments.

The use of multi-disciplinary analysis and optimisation process (MDO) to simulate a sufficiently complete flight mission by the inclusion of disciplines such as aerodynamics, structure and flight mechanics allows optimising the aircraft for maximal cruise range starting from a fixed maximal

take-off weight and a given fuselage. As an appropriate balance between accuracy and numerical effort, high fidelity modelling based on an Euler flow solver and a finite element solver is elaborated for the high-speed cruise part of the mission.

ATLLAS is carried out by a 13-member consortium. As major European manufacturers in the highly competitive high-tech field of aeronautical high-speed flight design and manufacturing, ASTRIUM (D), MBDA (F) and EADS-Innovation Works (D) provided the technical needs and application-specific expertise. One SME industrial partner, GDL (UK), developed a design method particularly suited to highly integrated engine/airframes and applied the method to the Mach 3 aircraft design. Another SME, ALTA (I), developed renowned skills and expertise in the field of high-speed flow experiments. The groups belonging to research centres (ESTEC (NL), DLR (D), ONERA (F), FOI(S)) and universities (Stuttgart(D), Munich (D), Southampton (UK) and UPMC at Paris (F)) are all working for long-time on specific issues of propulsion, combustion and aerodynamics with close contact to industry in bilateral, national and international collaborations. They provided basic knowledge, advanced investigation tools and unique testing facilities.

4. Novel Concepts for High-Speed Flights

Two aircraft configurations, suited to Mach 3 and Mach 6 flight are investigated. For both configurations, the major issues to be addressed from an aerodynamic point of view are sonic boom, aero-thermal loads, aerodynamic performance and fuels with good heat sink capability. The airplanes are being designed by two teams in parallel and integrated both almost by the same organizations, i.e. DLR, ESTEC, FOI, GDL, ONERA and UPMC. The selected design approach followed for each configuration has been completely different. The Mach 3 vehicle is the result of an inverse design strategy based on a method of characteristics where cruise efficiency and sonic boom mitigation have been the design variables. On the other side, the design of the Mach 6 vehicle is the result of applying a high-fidelity multi-disciplinary design optimization technique to an existing vehicle configuration. Here cruise range has been the optimization target. However, more than the configurations themselves the development and validation of the design-tools for both vehicles have required a major effort and constitutes therefore one of the major achievements.

4.1 Mach 3 Vehicle Design

In support of the design of the Mach 3 vehicle, the theoretical limits to cruise efficiency have been determined and a global approach to aircraft cruise performance optimisation was set out [9]. The strategy has been validated comparing predictions of cruise efficiency for Concorde and XB70. For the Mach 3 vehicle the analysis indicated that venting the exhaust in the lee of the wing and base of the fuselage will enable supersonic/hypersonic aircraft to have cruise efficiencies that are competitive with their subsonic rivals.

4.1.1 Vehicle Configuration

A vehicle configuration has been developed featuring a circular fuselage with nose intake and an internal high bypass turbofan. A water tight CAD model of the outer mold line was developed, together with a general arrangement showing the locations of primary system, fuel storage, cabins and undercarriage (Figure 1).

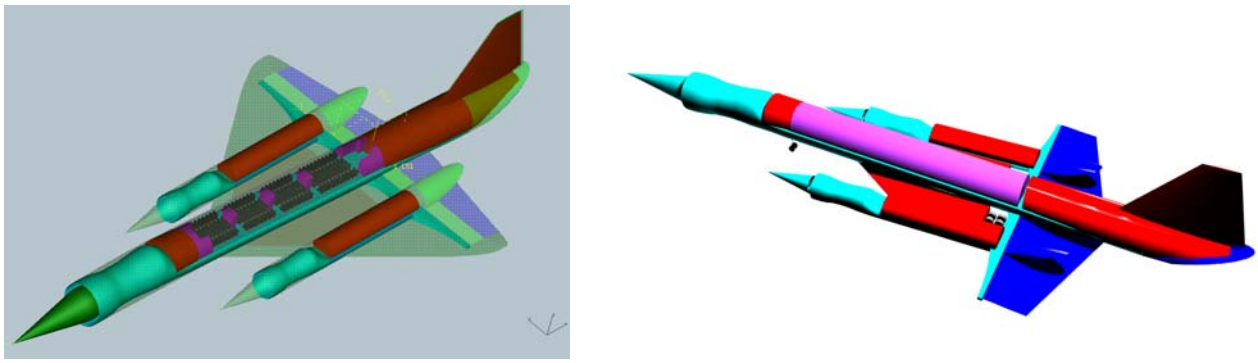

Figure 1: Mach 3 vehicle CAD-model (left); configuration with fuselage and wing skins off (right). Cyan: air flow path; blue: wing nozzle and thrust surfaces; red: fuel tanks; magenta: cabin.

The exhaust is ducted to the wing and fuselage bases. The wing has a high aspect ratio for good subsonic performance while drag due to thickness is strongly reduced by exhausting approximately two thirds of the propulsive stream from the wing trailing edge. Aerodynamic analyses for the Mach 3 configuration illustrated the feasibility of the propulsive-aerodynamic integration over a wide operational range. Particular attention is given to the expansion of the exhaust gases over the rear part of the wings in order to assess its impact on the overall vehicle performance over a wide range of flight Mach numbers (Figure 2).

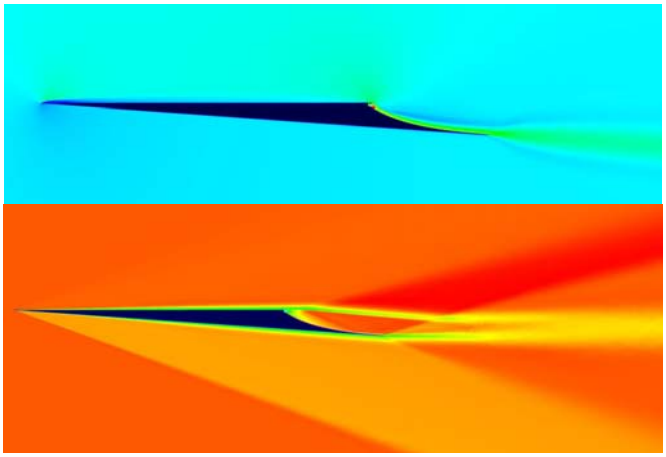

Figure 2: Mach 3.5 configuration: Mach distribution including exhaust expansion in the aft part of the wing: top: M=0.4, Alpha=0; bottom: M=3.5, Alpha=0.

4.1.2 Propulsion Design

Similarly, significant effort has been devoted to developing a propulsion model of the intake - ducted turbofan – air transfer duct and ramjet / afterburners (Figure 3). The models employs the compressor map scaling techniques of Kurzke [10] and ensures that the work provided by the choked HP turbine meets the core compressor requirements, and similarly that the LP turbine drives the bypass fan. Compatibility between bypass and core streams requires that their static pressure be equal prior to mixing. Also, an initial mass budget has been developed and used to perform a trajectory flight-out simulation. The vehicle undertakes a cruise-climb profile, with cruise efficiency above to 3.8, indicating a fuel burn during cruise of 160tonnes over the designed range.

4.1.3 Overall Performance

Finally, CFD predictions of the vehicle at cruise have been performed. Lift, drag and pitching moments have been determined from the calculated momentum fluxes, together with integration of the surface pressure and viscous forces. The nose to tail CFD simulation has provided an important confirmation of the design premise, namely that exhausting in the lee improves cruise efficiency in comparison to a conventional design whilst resulting in a vehicle with acceptable aeronautical characteristics. With an estimated gross take-off weight of 300tonnes, the simulation for the 200 seat aircraft results in an overall range of 10,000km (5,500Nm) with a 150t kerosene burn. But also the CFD simulations have shown an undesirable interaction of the wing nozzle flow field underneath the fuselage resulting in a reduction of lift of the overall concept, a relative high sonic boom signature of 105Pa (comparable to the 100Pa of the Concorde) and a marginally negative thrust-drag balance. Since parasitic drag from the fin was not included in the initial control volume analysis for the inverse design and also the real system has a greater ratio of wetted area to frontal area than originally assumed in the control volume optimisation, a future design should account for both effects.

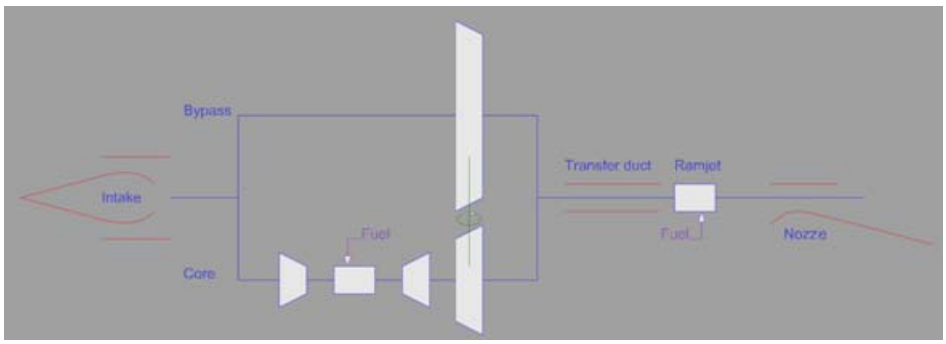

Figure 3: M3T engine flow schematic

4.2 Mach 6 Vehicle Design

For the Mach 6 vehicle, the departure configuration is based on the HYCAT 1A configuration designed by Lockheed in the late 70's. The intention within ATLLAS is to improve the overall performance of the vehicle in a semi-automatic way by means of a Multi-Disciplinary Optimization approach

4.2.1 Preliminary Vehicle Configuration

Parameters of different physical disciplines e.g. propulsion, structure and mission were provided by different ATLLAS partners and serve as input for the MDO process. Thus a complete mass budget, a propulsion table, mission database and geometry parameters are available. Within the ATLLAS project several MDO runs were performed whereas the last one includes all targeted disciplines. During the MDO process, for each configuration the following mass and structure analysis is performed:

i. determination of preliminary structural layout and structural masses;
ii. determination of maximum fuel mass;
iii. determination of a centre of gravity (COG) span depending on different fuel levels.

To reach these objectives the numerical method of finite elements (FEM) is used to increase result accuracy. During the ATLLAS project an initial FEM model was designed composed of shell and bar elements describing the basic structural layout. Furthermore element properties, material types and material groups were given to the model. Used materials are steel, aluminium, aluminium alloy and an aluminium-beryllium-alloy also known as Lockalloy or AlBeMet which is almost as stiff as steel but has a significantly lower density. The replacement of some parts of the fuselage cover by AlBeMet seriously improved the dynamic behaviour of the configuration. However the high costs of AlBeMet have to be mentioned which are not considered in the MDO process at the moment. The material properties were transformed to the MDO material library which was slightly extended by the C/C-SiC material for leading edges claimed by high temperatures. The material properties for C/C-SiC were provided by ATLLAS WP-3 and integrated to the structural process as anisotropic material. The arrangement of the several material groups is shown in Figure 4.

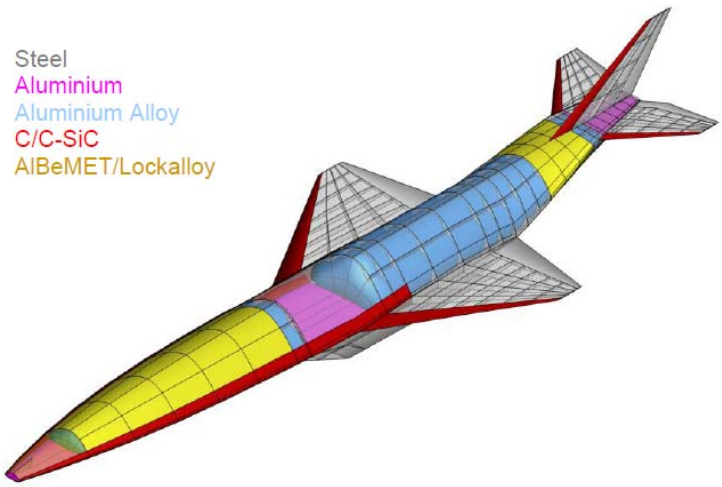

Figure 4: FEM Materials group.

4.2.2 Final Vehicle Configuration

The results of the final MDO are presented in Figure 5. The run was stopped after 520 iterations since based on former MDO runs no major improvements were expected beyond that. The time needed for a single iteration was between 3 and 5 hours while the overall time for one entire MDO process was 3 months.

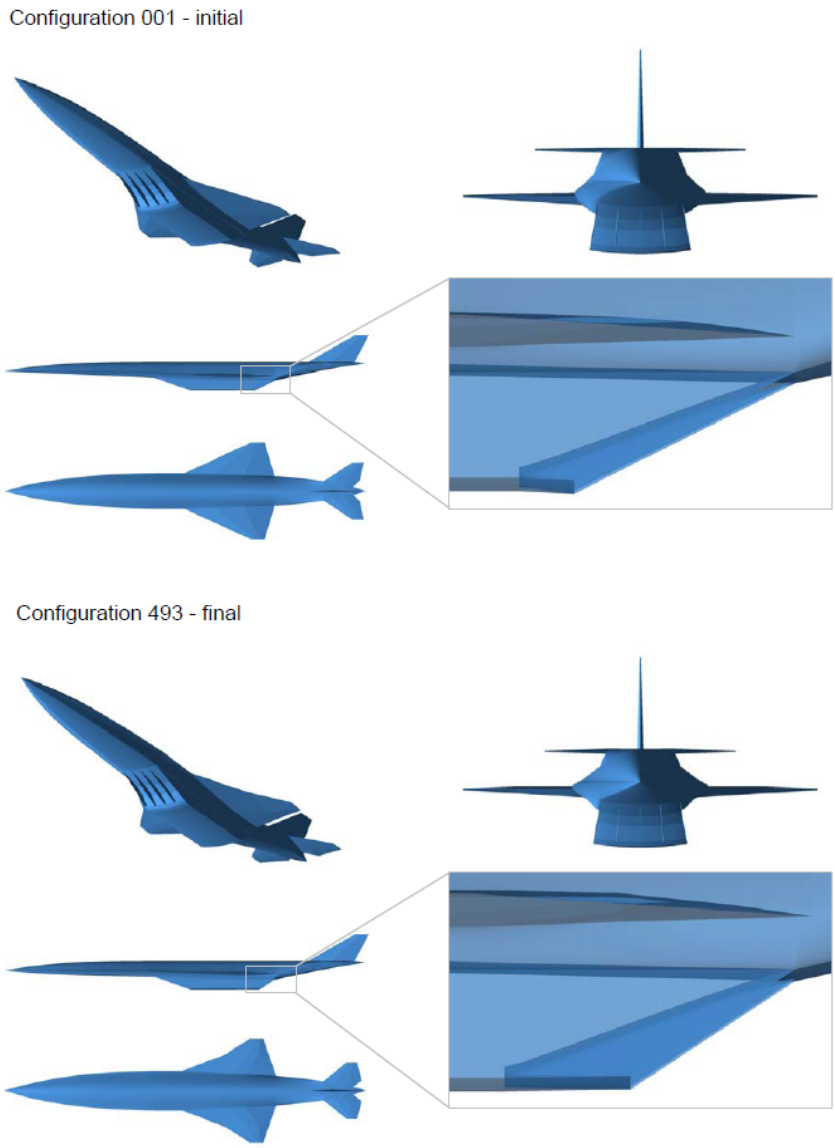

Figure 5: MDO current results: top: initial configuration, bottom: current configuration.

At first the changes of the configuration seem less then expected. The most obvious changes are the enlarging of the forebody, modifications of the wing and the horizontal stabilizer geometry as well as the nozzle design. There are also changes in the wing span width and wing vertical position given by the forebody leading edge z-component. Additionally the double-trapezium wing profile is strongly modified by moving the middle edges to each other. It seems that the profile shape is tending to a diamond profile. Additionally there are some marginal displacements of the nose and the wing tip position as well as a very small increase in tail thickness. During the MDO process for every configuration, a database is created containing more then 300 parameters to describe aerodynamic, propulsion, structural and mission performance. During the optimization the objective function is increased from 0.97 to 1.38. This means starting from a slightly penalized configuration the final configurations objective function is improved by almost 40%. The relative huge improvement is explained by the modification of the structural design and a better begin of cruise to end of cruise mass ratio and also by an improved interaction between propulsion system and aerodynamic. However, a final cruise range of 4250 km is still low. Respecting the considered reserve fuel and taking also the initial mission profile into account the maximum mission range of

the final configuration can be roughly estimated to about 7400 km compared to 6200 km of the initial configuration. The estimation is based on 1200 km for the accelerated climb, 1500 km for the descent and 500 km due to reserve fuel. The required hydrogen fuel on board resulted into a weight of 110tons. However the HYCAT 1A estimations of 9000 km mission range can not be confirmed within this work.

4.2.3 Structural Layout

Manoeuvre loads are considered for the structural analysis of the Mach 6 configurations. The first case is the symmetric pull-up, which represents also a gust-load. For the fuselage, a similar bending-case also occurs at touch-down. The load-factor at limit-load is assumed to be n_z=2.7. A second test combines the simultaneous loading of the stabilizer and tail fin (Figure 6). It is concluded that some additional local resizing might be needed. Further optimization, includes shifting mass from stiffeners to the surrounding skin to improve bending stiffness

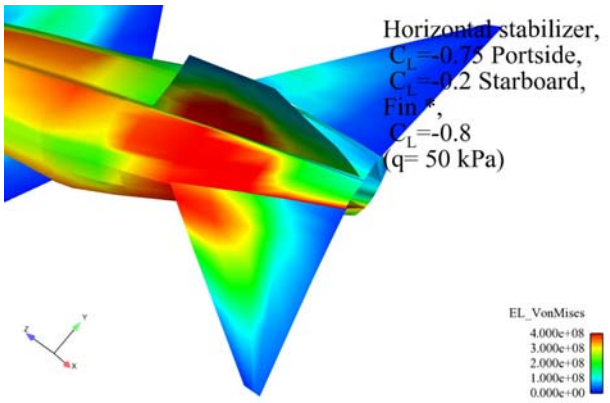

Figure 6: Stress-levels (von Mises) for a tail load case.

Further, a sensitivity analysis to the outer shape deformation has been carried out. The results show the most influent parameter being the first ramp deformation, with a visible effect on the intake aerodynamics as shown in Figure 7**.**

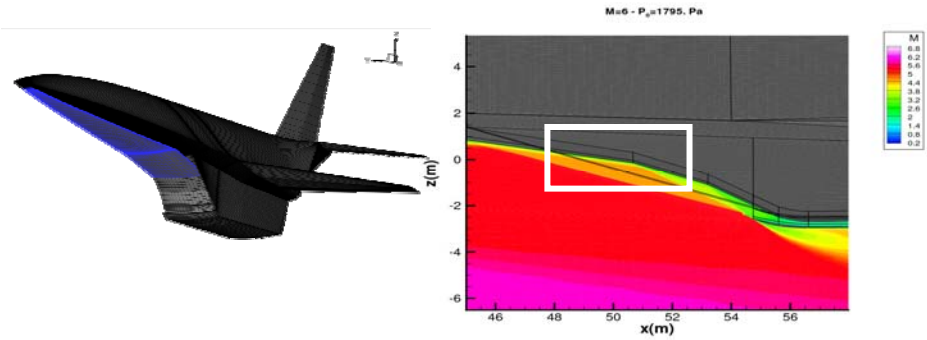

Figure 7: Sensitivity to forebody and ramp deformations for the Mach 6 configuration.

Due to the present results for future MDO processes the structural part of the MDO tool is one major point of interest. Indeed, here a fairly large and heavy aircraft has been analysed, which means that structural issues have a significant influence on the aircraft design (the structural weight is estimated to be about 30% of the gross-weight, whereas for instance the payload is about 6%). Large parts of the structure have their dimensions governed by stiffness requirements. The structural material chosen must of course be compatible with the expected temperatures for the structure, which depending on insulation and cooling may still be high. The stress-levels calculated over significant regions of the tail and rear fuselage requires further attention. The specific strength at room temperature of titanium and extreme high strength steels are about 50% higher than that

of aluminium. Not only the temperature limit for aluminium is much lower than steel and titanium, but its strength is also more drastically reduced at elevated temperatures. The choice made here to let stainless steel be representative for the specific stiffness seems appropriate during conceptual design and possibly during early stages of preliminary design. Beyond that a more detailed selection must be made due to different temperatures, thermal stress-levels and since dominant structural regions are designed for stiffness, but many parts will be designed under stress-constraints. The analysis performed here has indicated that a feasible design is likely to exist but a number of additional studies are needed (as for example the nozzle ramp displayed in Figure 8. More detailed design and analysis of a set of selected parts in different regions of the aircraft would improve data for the structural weight analysis. Such detailed design-work however requires more data about expected temperatures (cooling and insulation requirements). Within a more local design- and analysis study more attention can be given to design solutions to cope with thermal stresses and also maintenance issues.

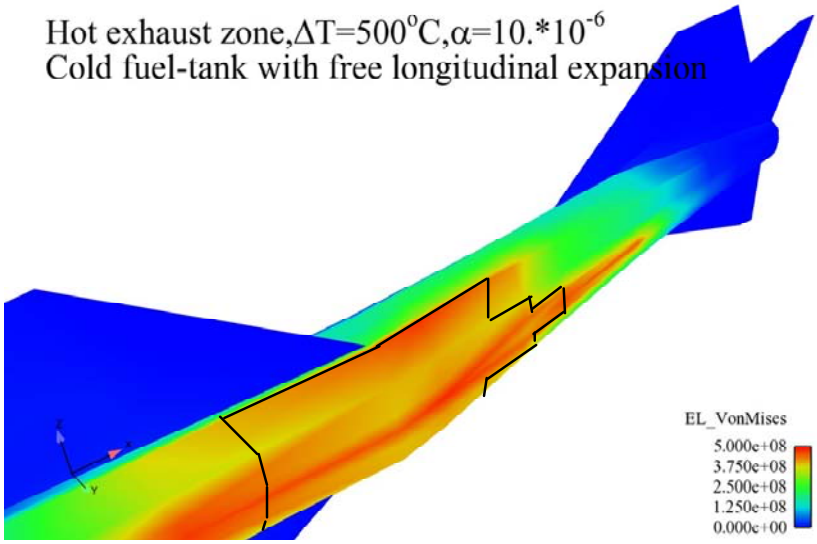

Figure 8: Stress-levels for a temperature-case of ΔT = 500°C.

The design of non-integral tanks for the Mach 6 reference configuration has been done using a new Multi-lobe Tank Extension Module, developed by DLR. This extension accounts for load factors, heat fluxes and fuel mass. The software is successfully used for a fast design of tanks that fit quite well inside the aircraft geometry.

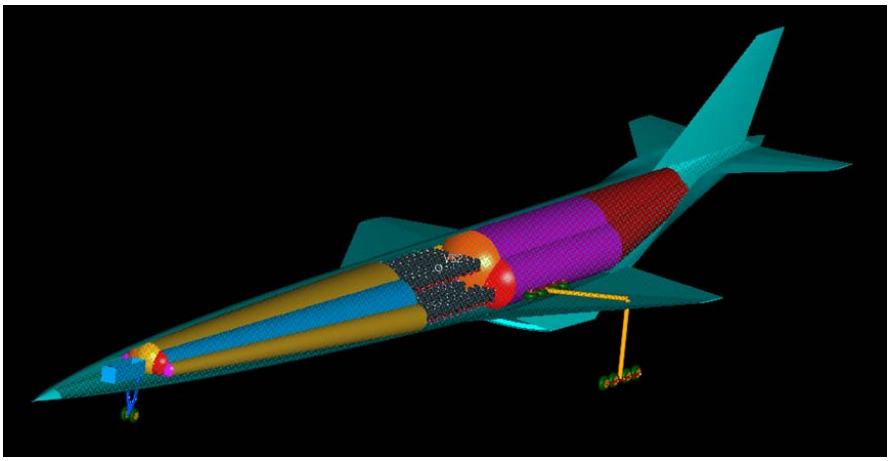

Figure 9: Automatic multi-lobe tank generation with aircraft fuselage constraint.

4.3 Sonic Boom Evaluation

4.3.1 Sonic Boom Prediction

During ATLLAS, there have been advances in the area of Sonic Boom prediction. The work has demonstrated that gravity is directly responsible for the attenuation of sonic booms as they propagate towards the ground, while the gradient in acoustic impedance has no effect on the wave strength. Therefore current sonic boom theory, although giving satisfactory matches with ground pressure measurements at low supersonic Mach numbers may be inconsistent at high altitude high flight Mach numbers. More specifically, gravity is omitted from the acoustic propagation equations and artificial acoustic impedance effects are erroneously introduced. Since Whitham's theory for bow shock strength has been compared with a Method Of Characteristics (MOC) calculation in a uniform atmosphere (without gravity) and found to be very accurate, the theory has been extended to include the effect of gravity and ambient temperature and the results are in near perfect agreement with the numerical MOC solution for the same case. Finally the method has been also applied to predict signatures of the Northrop-Grumman Shaped Sonic Boom Demonstrator (SSBD) showing good agreement with the experimental ground signature as is demonstrated in Figure 10.

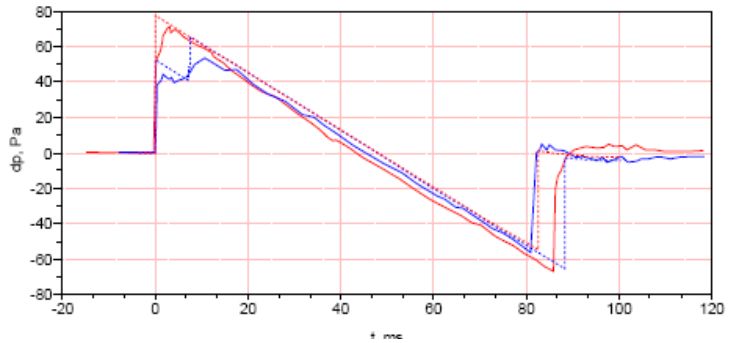

Figure 10: Measured (solid) and MOC (dashed) signatures for the SSBD (blue) and F-5E (red), assuming a ground reflection factor of 1.8

4.3.2 Sonic Boom Variability

For the Mach 6 configuration a statistical analysis about the variability of the sonic boom has been performed. Aerodynamic input data were the CFD near-field computation at the ratio R/L = 0.15 coupled with a multipole approach. The investigations done for the Mach 3 vehicle incites to retain the pressure signature extracted at the smallest distance from the aircraft for the sonic-boom propagation. Meteorological data were extracted from the ERA-40 database of the European Center for Meteorological Weather Forecasts (ECMWF) at year 1993, at two geographical points near Le Havre (France), which was the beginning of Concorde supersonic flight between Paris and New-York, and near Edwards AFB (California) where most of the recent sonic boom flight tests have been performed. The two points also are characterized by a very different humidity and temperature (and hence absorption) near the ground level, Le Havre being on the sea shore while Edwards is in the Mojave desert. The sonic boom propagation includes ray tracing in a stratified atmosphere with horizontal winds, nonlinear distortion, and atmospheric absorption due to classical and rotational viscosity, and molecular vibrational relaxation of nitrogen, oxygen and carbon dioxide. The sonic boom emitted in the vertical plan at 0° azimuth angle was computed every day for the Mach 6 configuration flying nearby 30 km altitude and for two headings (West and East). The width of the geometrical "carpet" has also been simulated systematically, along with some lateral distributions (one per month). The ground track sonic boom reaches an amplitude around 65 Pa, comparable to the one of existing aircraft, most of them comprised between 50 and 100 Pa (this last value typical for Concorde for instance). As expected, the rise time is somewhat larger at Edwards (mean value 1.7 to 1.8 ms depending on heading) than at Le Havre (mean value 1.0 ms) (see Table I) and in both cases shows a strong variability, the minimum and maximum values being separated by almost one decade (see Figure 11). ICAO standard atmosphere tends to slightly overestimate the sonic boom at the ground level. The carpet width also shows a significant variability, with larger values and more scattering at Le Havre due to stronger winds (see Table 1). Also heading towards East shows wider carpets and more variability due to more frequent downwind boom propagation. As a conclusion, the study estimated that the sonic boom from a

Mach 6 configuration would induce at the ground a sonic boom level comparable to existing supersonic aircraft but with a larger geographical area (due to higher Mach and higher altitude). As a consequence, overland supersonic flight by such a hypersonic vehicle is likely to be considered unacceptable by a significant proportion of the populations.

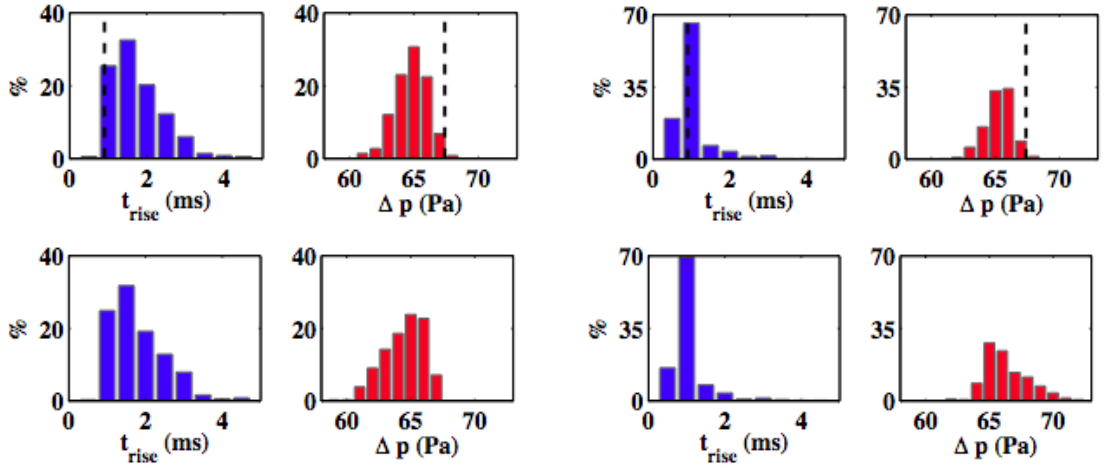

Figure 11: Ground sonic boom of ATLLAS Mach 6 configuration. Histograms for peak overpressure (in red – in Pa) and rise time (in blue – in ms) for Edwards (left column) and Le Havre (right column) for West (top line) and East (bottom line) heading.

Location	Heading	t_{rise} (ms)	t_{std} (ms)	Δp (Pa)	Δp_{std} (Pa)	W (km)	W_{std} (km)
Edwards	West	1.7	0.7	64.8	1.3	148.4	11.5
	East	1.8	0.7	64.4	1.6	157.3	15.7
Le Havre	West	1.0	0.5	65.2	1.1	153.6	19.2
	East	1.0	0.5	66.3	1.7	160.1	21.1

Table 1: Comparison of predicted ground track mean rise times t_{rise}, rise time standard deviations t_{std}, mean shock overpressures Δp, shock overpressure standard deviations Δp_{std} , carpet width W and carpet width standard deviation W_{std} for the ATLLAS Mach 6 configuration, two locations, and two flight directions.

Further, as other authors had previously identified cruise conditions is by far the part of the mission least prone to cause sonic-boom annoyance. The analysis of the mission profile of a hypersonic transport aircraft remarkably similar to the HYCAT 1A and the measured sonic boom data in a wind tunnel show that during descent the ground overpressure reached is two fold the cruise overpressure and during climb, even a four fold overpressure is reached. As the climb and descent phase of a mission are the legs most likely to pass over land, such very critical finding motivate to look for other type of measures to mitigate sonic boom like flow manipulation via magneto-hydrodynamic effects; via energy deposition (aero-jet or plasma spikes) or applying physical spikes. While none of them have had an important impact on the peak level of the overpressure, they affect the time-rise needed to reach the maximum. Here resides the potential of such measures since the time-rise is the primary source for the human-annoyance produced by sonic-boom. The study carried out for the Mach 6 vehicle shows that using energy deposition the time rise could be extended from 1ms to 30ms (!), but this comes at the cost of 100 MW which need to be deposited into the flow.

4.3.3 Sonic Boom Alleviation

Another application of energy deposition is the potential substitution of mechanical actuator devices like ailerons, rudders, flaps, etc. (Figure 12). Indeed, a 0.56 MW/m thermal deposition is able to cause the same force as a 5deg mechanical flap deflection but requires less total power (i.e. thermal and finite thickness drag power combined) than the 5deg mechanical flap deflection (in terms of finite thickness drag power). Further, energy deposition could be used to substantially change the location of the centre of pressure, depending on the position of the energy deposition.

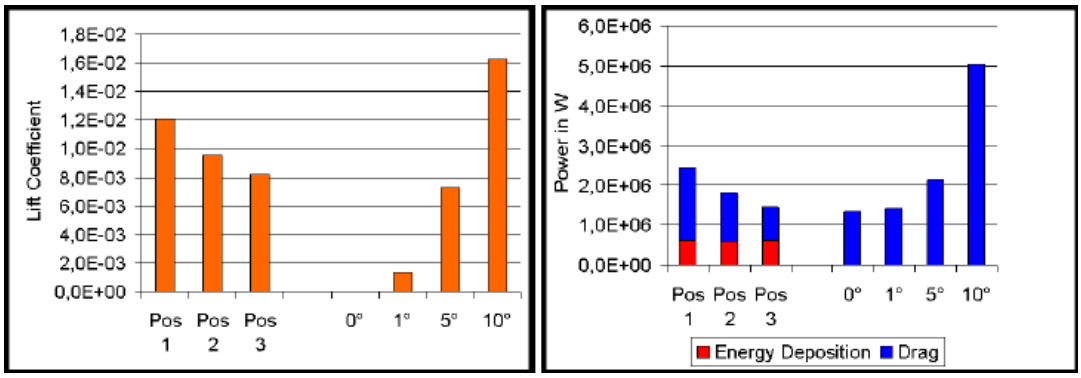

Figure 12: Comparison of produced lift and required power for energy deposition and mechanical deflection.

4.4 Aero-Thermal Environment

A logical follow-up of the study should now set up a more detailed materials requirement with respect to the vehicles thermal environment. Evolving from a more comprehensive study, the effects of the thermo-mechanics loads on vehicle aero-elasticity and structure dynamics can now be considered. From a pure thermal environment analysis, the materials investigated within ATLLAS satisfied both vehicles needs.

Further, for the ATLLAS Mach 3 vehicle, a power cycle employing cryogenic methane fuel has been developed to fulfil three roles within the vehicle: (i) provide cabin cooling from heat transfer through the external skin and internal air transfer duct; (ii) pre-condition the cabin ventilation air taken from the nose mounted intakes; and (iii) provide a source of auxiliary shaft power during cruise. Once the fuel has been used within the cycle, it is available for combustion, within the engines. Undertaking a typical flight over the design range (5,000Nm/9260km), 12t of methane fuel is required for the Mach 3 vehicle. The cabin insulation strategy has been carefully developed to ensure minimum weight of the insulation system, compatibility with the power cycle, and to retain the internal wall temperatures at 30^0C for thermal comfort. Figure 13.shows the cabin wall layout.

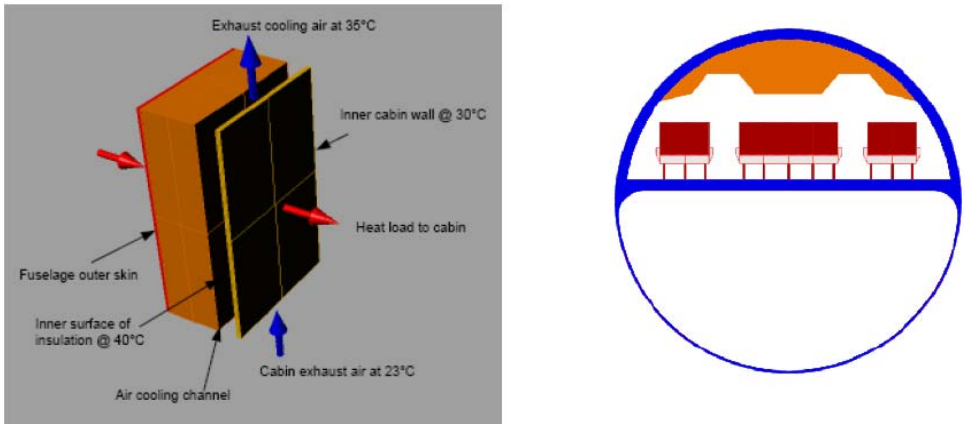

Figure 13: Mach 3 vehicle cabin cross section and proposed wall make-up. Fuselage outer skin and structural zone (red), inner insulation zone, air gap, for cabin return air and inner skin.

For the Mach 6 vehicle, fuelled by cryogenic hydrogen, it is observed that the latter provides nearly 10MW of latent heat sink capability in cruise. Environmental heat loads have been evaluated and an active cooling system is proposed for the cabin skin and a passive system for the fuel tanks.

Even with modest amounts of insulation, cooling requirements remain small compared to the cooling availability in the fuel. Furthermore, bleed air is available at nearly 2bar, eliminating the need of additional compression and therefore with a helium loop operating over a relatively modest compression ratio, large amounts of power are available.

4.5 Cruise and Fuel Efficiencies

It is quite clear that a lot of technologies need to be brought to a higher technology readiness level before one can even envisage kicking-off the manufacturing and operation of these types of vehicles. However, it is important that first the know-how and experience is put in place to assess whether or not any sort of high-speed concept has the required cruise performance. The study has shown that a cruise efficiency above three, i.e. L/D ratio times the propulsion efficiency, is recommendable for a long-haul cruiser. This can be achieved with the newly designed Mach 3 vehicle M3T (see Figure 14) which is also well above the Concorde's figure of merit. The Mach 6 vehicle is however rather disappointing even after a dedicated optimization process which brought it up with 10 to 20%. This doesn't mean a Mach 6 is basically not conceivable, but indicates rather that a 'classical' design as proposed by Lockheed is not recommendable. A different architectural design or an improved integrated engine design is needed to make it attractive. As this perspective is not out of scope, the Mach 5 A2 vehicle conceived during the LAPCAT project resulted clearly in a cruise efficiency above the critical value of 3. The better performance for the latter is mainly due to a thermodynamically high efficient engine concept.

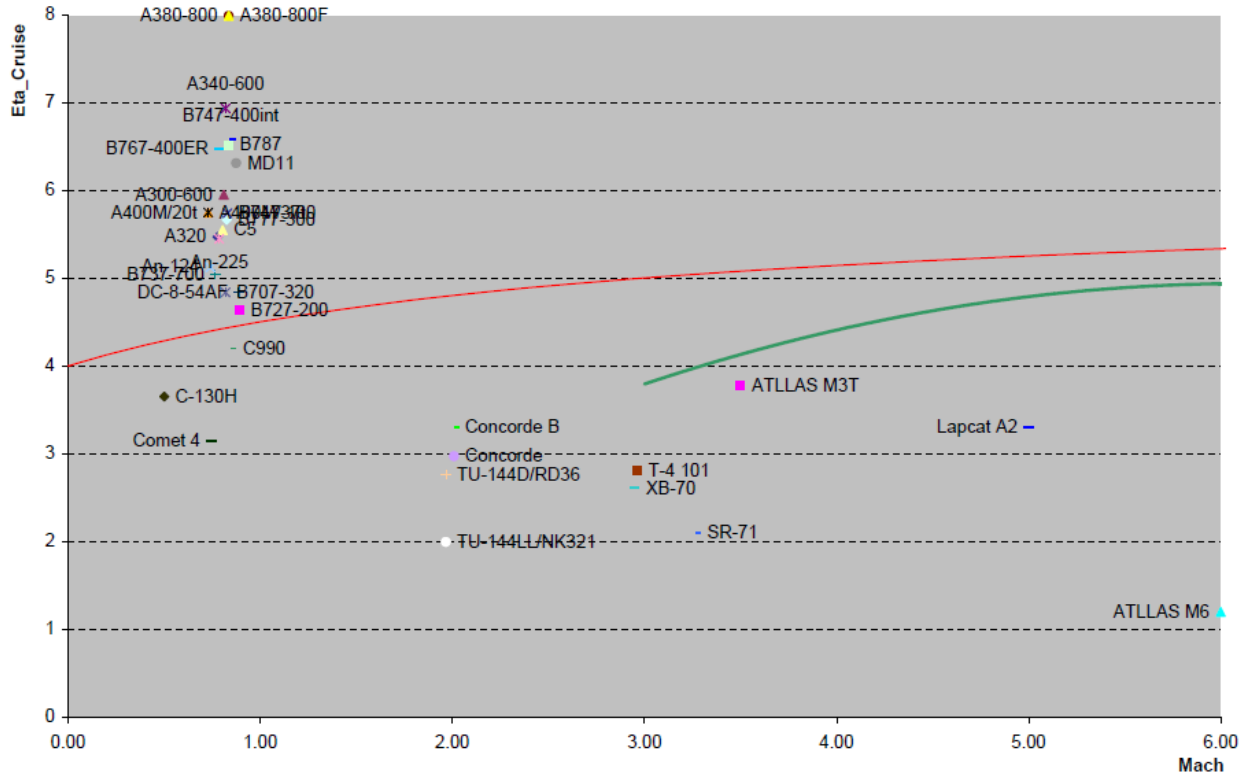

Figure 14: Cruise efficiency in function of flight Mach number for existing subsonic and supersonic vehicles along with the ATLLAS M3T (new concept) and the ATLLAS M6 (Optimized by means of MDO from the existing Hycat configuration of Lockheed).

In terms of fuel needs, the specific fuel consumption (sfc) is plotted versus Mach number in Figure 15. In a first approach, the sfc increases nearly linearly in function of flight Mach. A pure linear trend would be outstanding as this would result in the same total fuel mass consumption independent of the flight Mach number, whereas the travel time would drop inverse proportional. At first the sfc of the hydrogen powered LAPCAT A2 vehicle seems unrealistically low but as the specific fuel energy is about 2.8 higher than kerosene, an effective sfc would be quite higher but

still very competitive. This is due to the particular cycle used resulting in a nearly optimal thermodynamic efficiency. The sfc for the hydrogen powered Mach 6 vehicle, based on a nearly optimal design form Lockheed, is detrimental compared to LAPCAT A2 and the other HC-fuelled vehicles. As mentioned before, the poor propulsion-airframe integration and the rather conventional engine cycle are the prime causes of this disappointing performance.

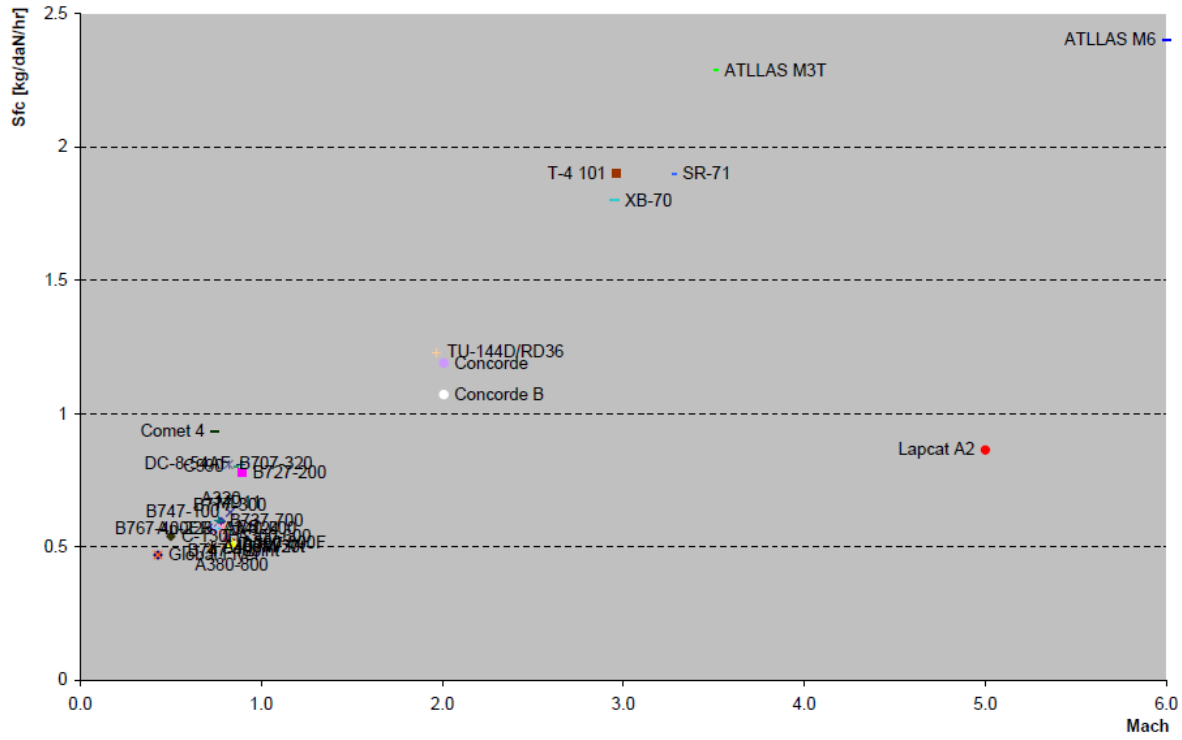

Figure 15: Indicative specific fuel consumption values for various sub- and supersonic aircraft in function of Mach number.

5. Lightweight Airframe Materials for Sustained High-Speed Flight

5.1 Material Requirements

High-speed aircraft are exposed to high thermal and mechanical loads. Especially the nose structure, wing leading edges, air intakes etc. reaches temperatures which require special heat resistant materials, structural concepts and optional cooling devices. As the requested aerodynamic performance for an aircraft focuses on a high aerodynamic lift to drag ratio requiring sharp leading edges and rather thin wing or stabilizer structures. The utilization and implementation of both of these requirements demands a detailed investigation of lightweight airframe materials including material design, coatings and determination of basic material properties withstanding high temperature requirements (Figure 16). This includes various tests on material samples to determine temperature stability, chemical resistance to the expected operational environment, mechanical stability and required additional physical properties. Three general classes of material investigation are considered: metallic hollow-sphere packings (HSP), Ultra High Temperature Ceramics (UHTC) and Ceramic Matrix Composites (CMC). Each of these is addressed below.

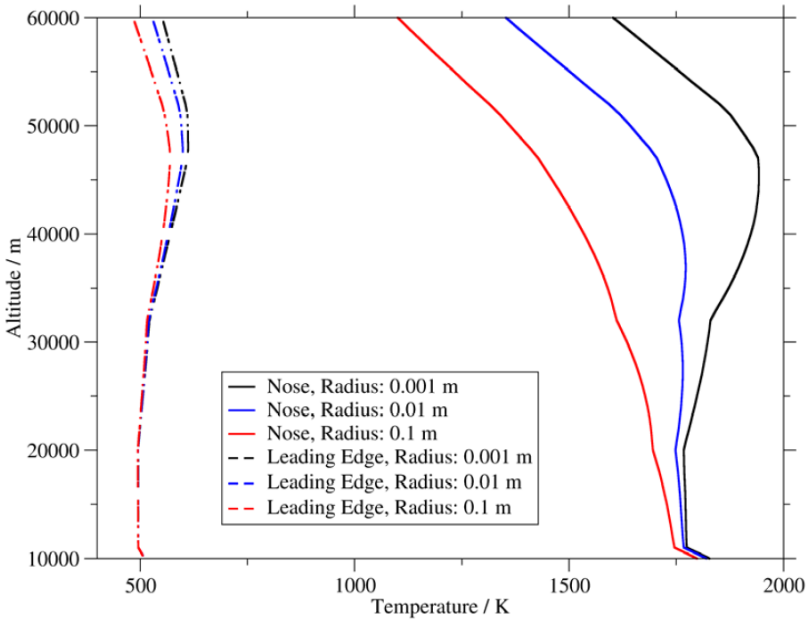

Figure 16: Radiation equilibrium wall temperature at stagnation point, Mach 6, ε = 0.85, Λ = 65°.

5.1 Hollow Sphere Packings: HSP

Various methods fabricating cellular solids, mostly foams have been investigated in the past. Most effort has been spent in the field of aluminium foaming processes. An entirely different concept to manufacture cellular solids is the approach via hollow spheres. Employing the hollow sphere technology, structures can be designed virtually to application needs. In contrast to classical foaming processes, there are no restrictions with regard to material selection (melt viscosity and stability). The powder metallurgical approach is applicable to any metal or even high performance alloys. The hollow sphere technology allows high degrees of porosities, reproducible properties and fair process control, structural regularity, excellent noise absorption and low weight.

The principal feasibility of metal hollow sphere based components for high-speed transport vehicle and propulsion systems are evaluated by ONERA on an engineering test sample level. The fabrication techniques for hollow sphere structures are adapted to the application requirements with regards to materials, densities and thermal properties [13]. In parallel, fabrication technologies for panels with hollow sphere cores are developed (Figure 17). This includes screening of suitable

joining techniques (brazing, diffusion bonding) and relevant test methods thereof. Establishing suitable joining techniques for hollow sphere structures is a crucial step to supply components in sizes relevant for the envisaged application. A second axis aims at determining the mechanical and acoustic absorption properties of lightweight high strength structural panels for high temperature structures in nickel based microsphere panels.

In parallel a Finite Element based model is developed to characterise the mechanical behaviour under compression of hollow spheres packings (Figure 17). Emphasis is put on the influence of the architecture of the packing on its mechanical response. Calculations are conducted on infinite simple cubic (SC-), body centred cubic (BCC-) and face centred cubic (FCC-) packings by applying planar, uni-axial compressive loads [14]. It turned out that the behaviour of Hollow Sphere Packing (HSP) is mainly governed by the localised plasticity in the neighbourhood of meniscus ends for small strain levels; for higher strain levels, buckling of hollow spheres and self-contact between spheres occurred. Furthermore, the influence of the geometry and type of a HSP has been analysed. Like for other cellular materials, the effective mechanical behaviour of HSPs strongly depends on their compactness as well as on their relative density. For instance, the moduli increase with the compactness of the packings, which indicates that they are highest for FCC-like and lowest for SC-like packings. In order to estimate the sensitivity of the effective material behaviour of the packings, a calculus of variations for the constitutive material's behaviour is performed. It constituted, that a pure plastic behaviour for the packings does not exist, even for smaller strain levels causing a local plastic contribution. Additionally, investigations on the effect of defects like e.g. a dispersion of the geometrical packing parameters and varying the solicitation rate were performed including an elasto-viscoplastic behaviour for the constitutive material.

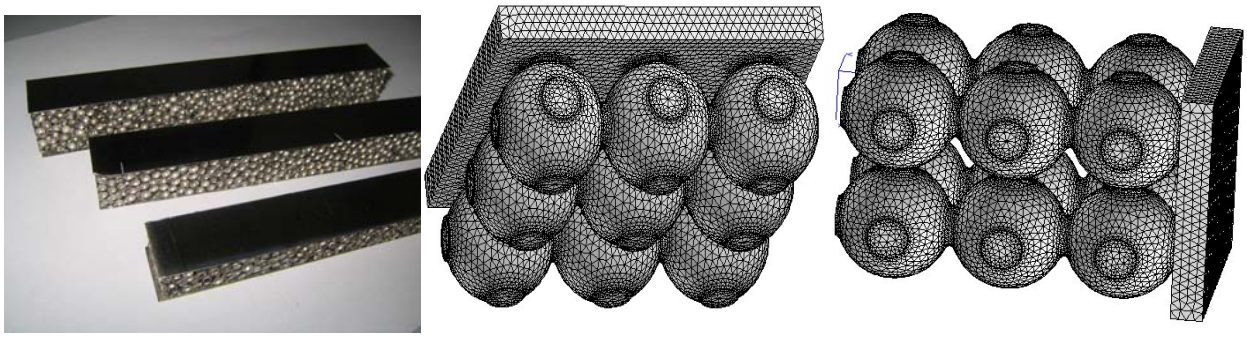

Figure 17: Sandwich panels with a HSP core for structural testing and its mechanical modelling for its compressive behaviour. Left: 6x6x2 hollow spheres with t=0.56mm; right: 4x4x6 hollow spheres with t=0.56mm

5.2 Ultra High Temperature Ceramics: UHTC

The interest in UHTCs has grown in the past years, especially in the US and in Italy. However, their application in aerospace is limited and demands for further exploration. Just two experiments under real flight conditions were undertaken with the Sharp Hypersonic Aero-thermodynamic Research Probe-Ballistic experiments 1 and 2 (SHARP-B1, 1997, and SHARP-B2, 2000). Oxide materials are, at best, intrinsically resistant to oxidation. The manufacturing and investigation of ultra high temperature composites within the project are based on a mixture between transition metals, borides and carbides. The interest of such associations is to promote the formation of dense refractory oxides like ZrO_2 and HfO_2. The most suitable way to produce sharp edges is to manufacture monolithic parts using hot pressure sintering of an appropriate mixture of powders. Monolithic UHTC inserts could be also applied in composite structures. Another challenge to succeed in this field is to achieve a sufficient level of toughness to overcome the brittleness of ceramic materials.

The work conducted by ONERA further developed the hot pressing sintering for three selected material compositions. In order to reduce contamination and to obtain the purest compounds possible, the attrition process and times were improved. The dimensions of the manufacturable flat

samples could be enlarged up to 68x68 mm². Additionally discs and parallelepipeds were machined. In order to prove feasibility, very thin structures (thickness 1.9 mm) with minimal nose tips (radius app. 0.15 mm) were manufactured (Figure 18). Specific samples were manufactured to investigate thermal and chemical characteristics at the arc-jet testing facility L2K of DLR Cologne [15].

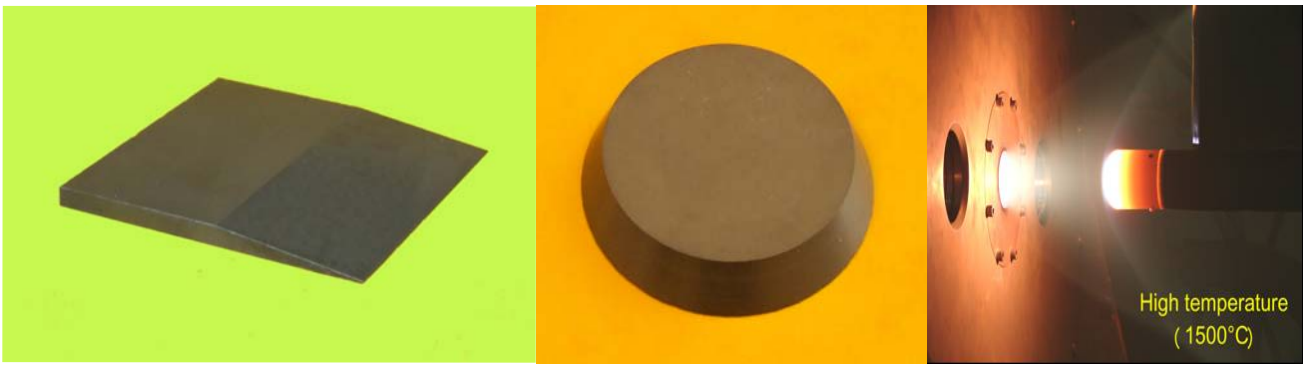

Figure 18: UHTC air intake prototype (40x40x1.9mm3); arc jet sample Ø 26,5; thermal and chemical tests at the L2K facility of DLR.

Mechanical investigations determined the hardness indicating high values close to tungsten carbide. Measurements of toughness revealed that this parameter is very limited like common silicon carbide. Three point flexural tests showed that the flexural stress were equal or higher with increasing temperature, similarly for the flexural strain but nevertheless a significant decrease of modulus. Additionally, the thermal expansion of UHTC material was determined for a range between 20 °C and 1250 °C at argon atmosphere along with the emissitivity.

5.3 Ceramic Matrix Composites: CMC

The application of ceramic matrix composites for leading edges and air intakes are investigated by three DLR institutes (BK, WF, AS-WK) and FOI. Its application demands a densified material with high thermal conductivity and emissivity. Hence, the fibre orientation and matrix composition should be well adapted along with adequate coating procedures to provide optimised surface properties. Chosen CMCs are C/C-SiC and OXIPOL, manufactured by DLR-BK, and WHIPOX by DLR-WF. Structural tests at DLR-AS-WK focus on a generic but representative design and manufacturing of a sharp leading edge including an interface to an adjacent structure. This sample needed to consider structural and system aspects like joining technique to a cold substructure and sensor integration. One major objective is to fit this structural sample within an arc jet test facility for a test within high-speed gas flow conditions.

Though the application of C/C-SiC or C/SiC for re-entry vehicles is state of the art due to the material's excellent thermo-mechanical behaviour, their service-life is low in comparison to the requirements for hypersonic aircrafts, e.g. extended 25,000-cycle service-life. C/C-SiC and WHIPOX were already tested during SHEFEX as thermal protection system of a hypersonic experiment. In general, oxide ceramic based materials offer a wider framework to tune their material characteristics to the envisaged application. As WHIPOX has low emissivity characteristics, a dark coating based on spinel phase with high emissivity is developed and tested in the arc jet testing facility L3K. Different fibre orientations are investigated (1D = $\pm$3°, $\pm$15° and 0|90°) to determine Young's modulus, interlaminar shear strength, bending strength and notching sensitivity [20] below. Also creep tests are performed at 1100 °C. Unfortunately, creep/fatigue tests for the non-oxide CMCs could not be performed. For optical characterisation, FOI measured the reflectance and transmittance at room and high temperatures [17] below.

5.4 Material characterization: temperature dependancy

For the characterization of high temperature materials, usually a trade-off between specific strength, oxidation resistance, costs and reliability has to be considered. The inputs for the specific strength of CMCs, given as the ratio between tensile strength and density, subjected to earth's gravity can be found in D3.0.1. For HSPs and UHTCs, the tensile strength was not determined, so neither the specific strength could be built. Figure 19 shows the specific strength vs. temperature of damage tolerant, dense CMCs compared to metal alloys.

Non-oxide materials such as C/C-SiC seem to be stronger than oxidic ones (OXIPOL 4x and WHIPOX in several variants). For small winding angles of WHIPOX, the material's behaviour is mainly fibre-dominated and the strength increases. It can be concluded, that ceramic composites like C/C-SiC are very favourable as they don't loose their strength at high temperatures which is in clear contrast to the behaviour of metal alloys.

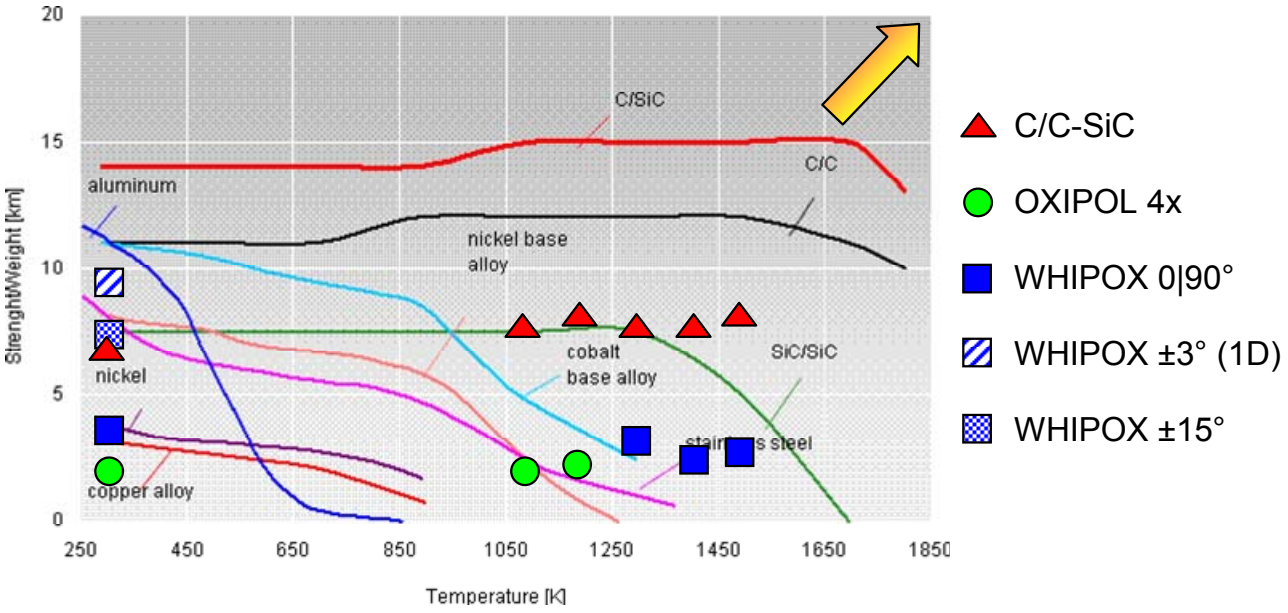

Figure 19: Specific strength vs. temperature

Finally, a leading edge model is manufactured in order to study the thermal and chemical characteristics of a representative leading edge in an arc jet heated flow. Since the sharpness of the leading edges is limited by the material's manufacturing process, a leading edge nose radius of 2 mm was defined as baseline for all materials (C/C-SiC, OXIPOL, WHIPOX). Since there is no specific limitation for C/C-SiC, a very sharp leading edge is manufactured to study directly the effect of sharpness (Figure 20). FOI provided a numerical simulation for the comparison of the experimental tests. The structural part is modelled using a FE method. For the fluid-structure analysis, a modal representation of the structure is investigated in order to provide the model reduction needed to manage a large scale coupled analysis (Figure 21).

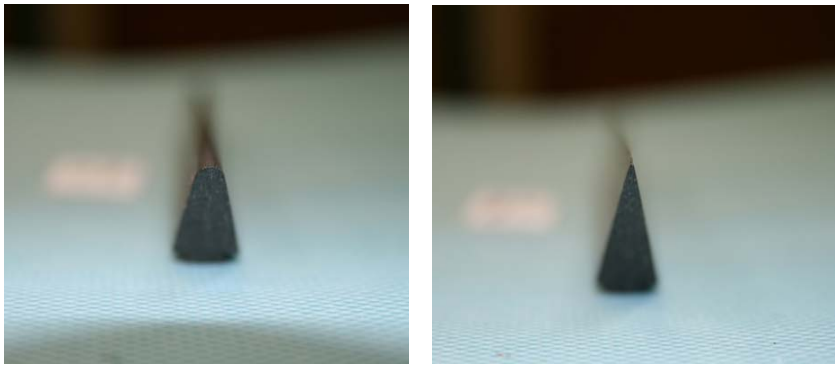

Figure 20: C/C-SiC leading edge with radius 2 mm (left) and sharp-edged (right)

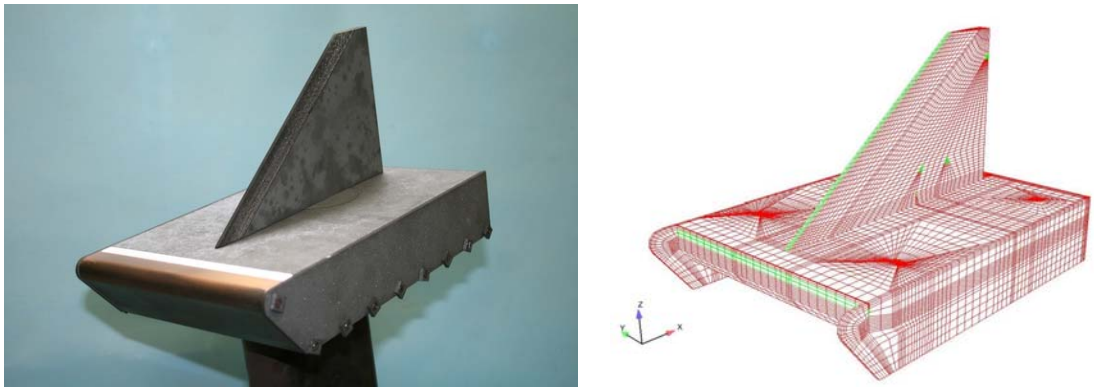

Figure 21: Leading edge model and its mesh for numerical simulation at FOI

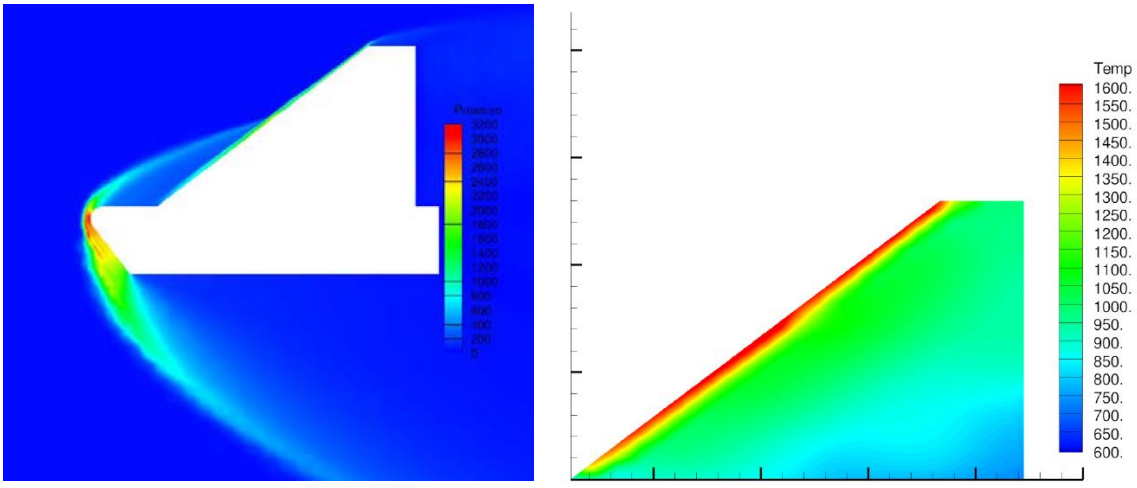

Figure 22: Simulated pressure contour along the symmetry plane (left picture) and simulated wing temperature distribution for OXIPOL (in Kelvin) at α = 5°and δ = 0° (right picture).

The overall outcome of the numerical validation is fairly good, despite some simplifications made, and the dependence of the temperature profile on the flow direction is well depicted by the simulation model. The surface temperature near the location of the bow shock is affected by the different angles of attack. The central part of the wing is relatively far away from the cover plate where the bow shock is weak for the considered angles of attack. Figure 22 shows the pressure contour along the symmetry plane of the model for *α = 5°and δ = 0°*.

6. Increased Engine Thermal Efficiency: Novel Cooling Concepts

In this work package, activities were focused on increasing the combustion temperature by using lightweight materials and novel cooling concepts of the combustion chamber liners. Different fuels were taken into account, which are required for the studied aircraft concepts: kerosene and cryogenic fuels. Both high-pressure (aerojets) and ramjets based combustion chambers were used as a test bed to deal with realistic operational gas flow conditions. Different cooling techniques were investigated under a wide parameter range: film, effusion, transpiration and regenerative cooling. The thermal performance was investigated and a comparison to the simulation results was performed. A special work package was dedicated to the forecast of NOx emissions and the investigation of possible countermeasures to reduce these. Detailed information is reported in [16].

6.1 Cooling of High Pressure Combustors

To perform the experiments on the different cooling techniques and materials, TUM designed and commissioned a single-element subscale combustor tailored to the requirements of the partners involved in the work package [17]. Film cooling experiments were performed with gaseous nitrogen and kerosene. The operating envelope stretched from 20 bar chamber pressure up to 60 bar. This allowed assessing the influence of the fluid properties with respect to the critical pressure of 23 bar for kerosene on the cooling performance.

Film cooling experiments were performed to bridge gaps in the open literature data: for the foreseen range of gas temperature and pressure, no data was available to anchor design tools. State of the art and existing models were expanded to define the configurations to be tested [21] below.

Based on experience obtained from a transpiration cooled ceramic combustion chamber for rocket engines, it seems to be possible to use a similar cooling technology for high speed airbreathing engines. With less air used for cooling, higher combustor liner temperatures are obtained in the order of 1800K. With CMC turbine vanes able to cope with these higher combustor exit temperatures, the overall thermal efficiency increases.

The main focus for the purely transpiration cooled ceramics provided by DLR was put on oxide ceramic based materials for combustion chambers. Besides their high temperature stability, the specific weight and their possibly oxidising stability offer a wide range of possible applications. In addition to the very high gas temperatures and pressure within the engine (combustion chamber, expansion nozzle etc.) the chemistry and gas composition (O2, H2O, CO2, H2, N, CH...) affects the structure of the material. Within this area, oxide based CMCs combined with active cooling are promising candidate materials. For comparison, a C/C material has also been used for transpiration cooling tests. This material allows for higher operational temperatures provided that the transpiration coolant flow successfully protects the carbon matrix from oxidizing combustion products, i.e. free oxygen or water vapour as products from the combustion process.

The principle of this cooling technique is to create a gas flow from the cold substructure to the hot surface directly through the porous material itself. Thus, in addition to the direct cooling effect, the boundary layer at the surface is influenced reducing the convectional heat transfer and chemical reactions. In contrast to the above mentioned current development of the C/C based transpiration cooled burning chamber for a H2/O2 rocket engine with fuel rich burning conditions, engines for high-speed aircraft are designed for optimised efficiency resulting in a lean, oxidiser rich burning condition. Thus, oxidation-resistant materials are of prime concern.

An alternative approach to increase the operating temperature of combustors is pursued by Astrium and MBDA France with the PTAH-SOCAR design [23]. Here, a 3D-C/C material is covered by oxidation protection coating. The resulting CARBOTEX^{SI} material is used to manufacture rectangular or axisymmetric coolant ducts. As the material is not gas tight towards the combustion chamber, a certain amount of coolant acts as transpiration coolant.

Additional activities addressed the investigation of high-temperature alloys with respect to their oxidation resistance and the development of possible protective coatings.

6.1.1 Heat Flux Measurements

Most of the hot fire experiments were used to provide data for the development of a heat flux sensor being capable to withstand the demanding environment of a combustion chamber with minimum geometric design constraints. DLR Cologne developed a heat flux sensor concept based on a null-point calorimeter concept. The resulting design is characterized by the small sensor dimensions and is congruent with the constraints and requirements coming from the planned operational domain as well as from the test specimen. The design of the probe was verified based on Ansys FEM simulations, taking into account the setup in the foreseen combustion chamber. Afterwards, it was put to test in an oxidizer rich combustion chamber setup at TUM used in work package 4.4. Figure 23 shows the design of this sensor and the results of the Ansys simulations.

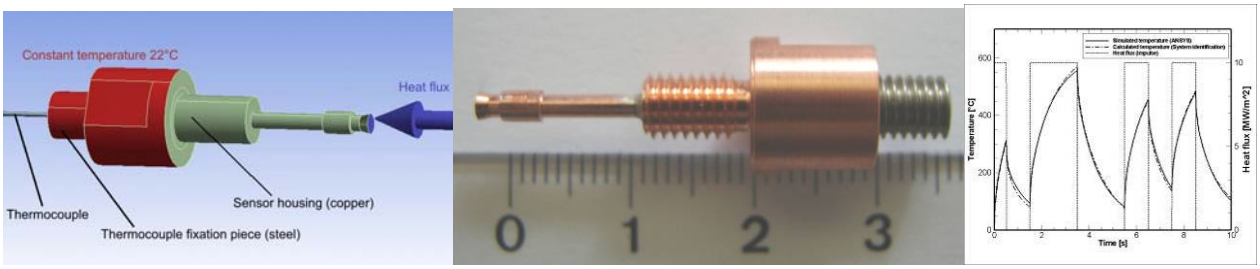

Figure 23: DLR Cologne heat flux sensor: ANSYS model, first probe and temperature sensor response

In order to compare the data recorded with this heat flux sensor with reference data from heat flux sensors applying a different measurement principle, test data was also recorded with a reference sensor designed and calibrated by DLR. The design and commissioning of this second sensor was done by DLR as no commercial available heat flux sensor could meet the requirements of the specific application on the TUM combustion chamber test bench. The measurement principle of this second sensor is based on the temperature gradient in a material with a given thermal conductivity. The design is illustrated in Figure 24. The sensor was calibrated in DLR's L3K test facility and hot fire tested in the single-element combustion chamber at TUM.

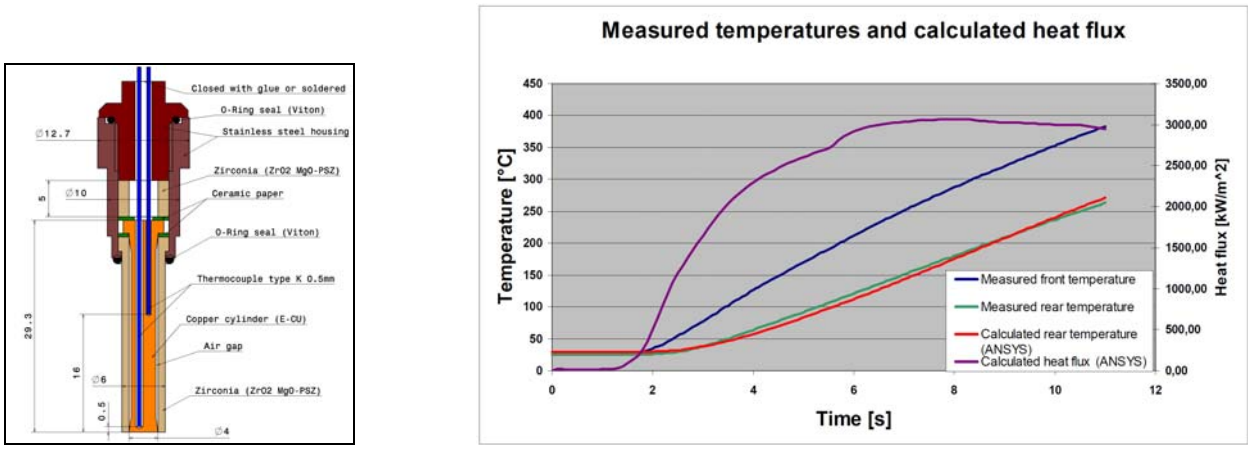

Figure 24: Design of reference heat flux sensor (left) and L3K windtunnel test results with 3000kW/m2 heat flux load

6.1.2 Film Cooling

TUM-LFA investigated also film cooling under steady-state conditions i.e. in combination with water-cooled combustion chamber segments (convective cooling) [21]. Furthermore, TUM designed and commissioned a water cooled single element combustion chamber setup to be used as reference in the experiments.

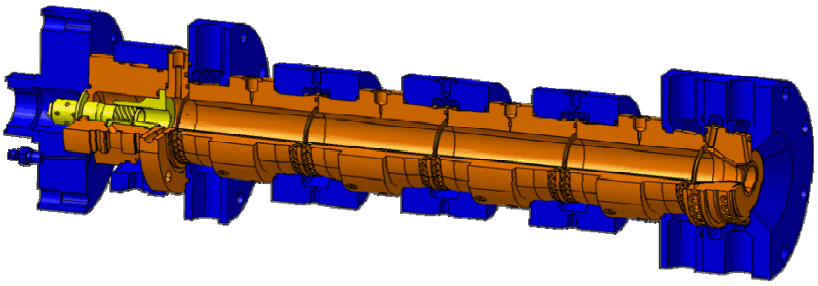

Figure 25: Single-element combustion chamber designed and characterized for ATLLAS

The film applicator used for the film cooling experiments is shown in Figure 26. The design of the film applicator allows the integration of both heat sink as water cooled combustion chamber segments. The setup consists of three parts, an outer ring (base plate) comprising the manifold and feeding system, a ring in the middle (spacer ring) which defines the film application slot height and a counterpart comprising the film lip and space for sealing.

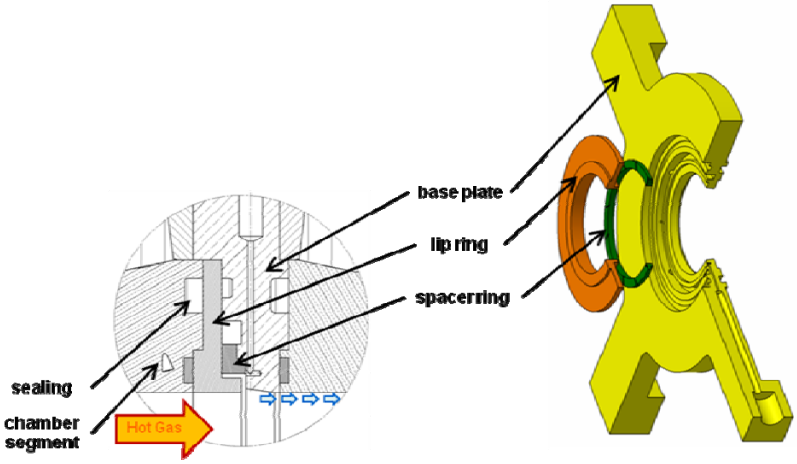

Figure 26: Film applicator details (sketch and 3D cut-away)

Tests have been performed at chamber pressures of 20 bar, 40 bar and 60 bar with injector mixture ratios varying between 2.7 and 3.4. The cooling fluids were gaseous nitrogen GN2 and kerosene Jet A-1, whereas mass flow rates have been varied between 3 g/s and 35 g/s or film mass flow ratios of 5 % up to 23 %, respectively. Altogether 17 successful hot tests have been performed. 73 load points have been recorded for evaluation.

Analysis of the heat fluxes showed that for nitrogen moderately high mass flows are required i.e. μ=15% to lower heat flux density by approximately 20% over a segment length of 95 mm. With kerosene the heat flux density can be significantly lowered (30% up to 60%) with a high dependency on the mixture ratio can be found.

In Figure 27 the heat flux densities for the four water-cooled chamber segments and the water-cooled nozzle segment are summarized for different load cases. The main driving factor for different heat flux densities is the combustion pressure. Within the range investigated, the influence of the mixture ratio is approximately in the same order as the heat flux uncertainties are (~10…20 %). As expected, higher film coolant mass flow rates lead to lower heat fluxes in the third, fourth and the nozzle segment.

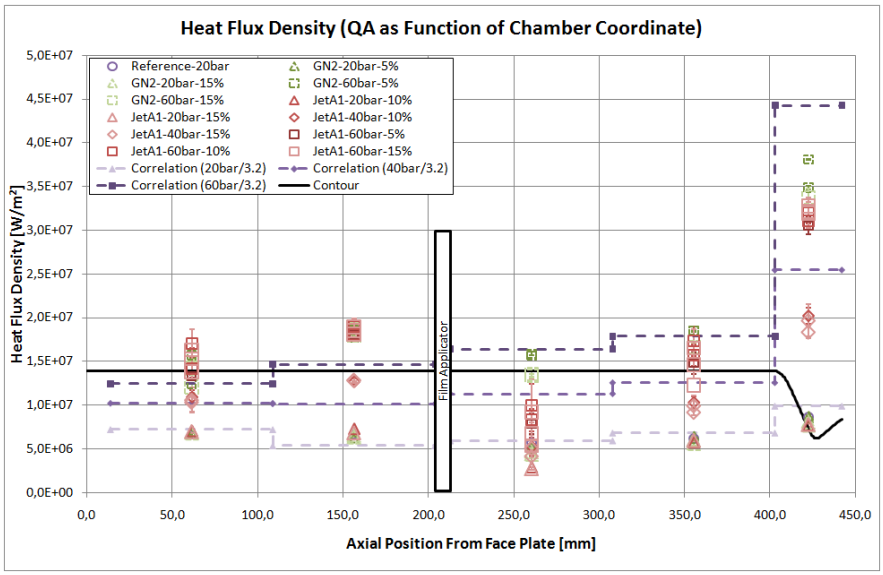

Figure 27: Heat Flux Density over Axial Position (Mean with RMS)

6.1.3 Transpiration Cooling

DLR BK in Stuttgart manufactured different CMC materials for transpiration cooling tests performed at TUM [19] and ITLR. For the TUM setup, axially symmetric combustion chamber segments were required, whereas at ITLR flat samples were tested. Within two separate test campaigns, test specimens made of C/C, Whipox and Oxipol were tested successfully.

Figure 28: WHIPOX liners manufactured by DLR for transpiration cooling tests at TUM, from left to right: WHIPOX, C/C, WHIPOX, OXIPOL

The test data was used to optimize the design of the segments and to validate the numerical tools. From test to test, permeability measurements were performed to trace any change of the material's behaviour, see Figure 29. Extensive investigations using computer-tomography (CT) were used to document the degradation of the material and to develop possible scenarios to explain the damages found on the samples after testing, e.g. Figure 30. A thorough assessment of the achievements and the weak points was performed by DLR to further mature this technology towards an application in an airbreathing propulsion system.

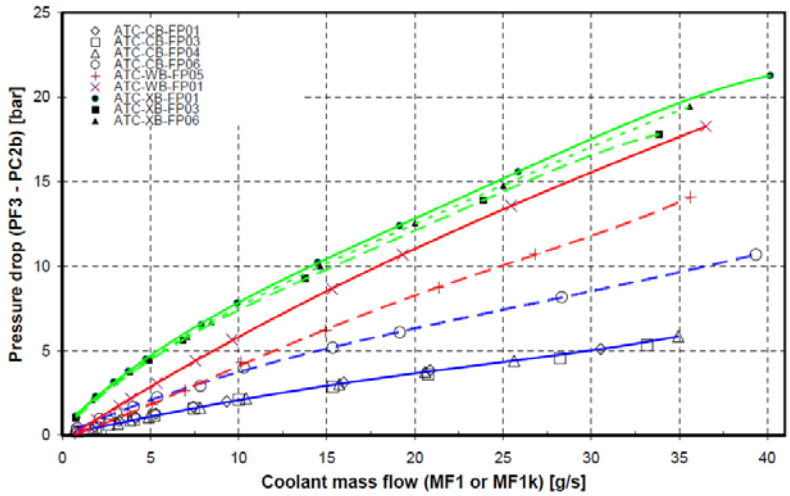

Figure 29: Measured pressure drops of CMC samples before, in-between and after hot run tests

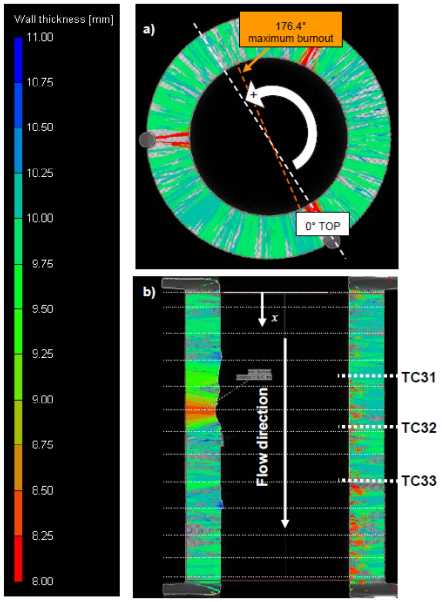

Figure 30: OXIPOL, sample (left) and CT section definitions at dedicated (a) circumferential (as seen from front face to exit) and (b) axial positions

In addition, several test cases were simulated by TUM's tool THERMTEST based on a 3D mesh. Here, a modified boundary layer model was integrated which takes into account transpiration. The measured CMC thermocouple temperatures could then directly be compared to simulated values. Unfortunately, large deviations exist here. Nevertheless, the simulated CMC wall temperatures give a rough estimation on e.g. too demanding load points or promising coolant mass flows. As it is not possible to directly measure the CMC surface temperature at zero blowing, the temperatures were calculated analytically. Together with analytically determined cooled wall temperatures, cooling efficiencies between 0.60 and 0.93 were determined.

Parallel to the hot fire test campaign, all DLR materials were characterised with respect to their anisotropic permeability properties at DLR in Lampoldshausen. In this experiment, different fluids were used to characterize the pressure drop behaviour of the material. The data were fed back to a numerical model, in which by means of a regression analysis the characteristic coefficients of the materials' permeability were determined.

6.1.4 Regenerative Cooling

Astrium and MBDA designed and manufactured samples of CARBOTEX^{SI} material in the PTAH-SOCAR layout (Figure 31-Figure 32) [23]. Semi-empirical and available CFD-tools were used to prepare the test. As with the other CMC materials, the convectively cooled samples were tested both at TUM as at ITLR. For the tests at TUM, it was originally planned to have an integral CMC design to be able to operate the cooling circuit up to outlet temperatures at which supercritical kerosene is subjected to pyrolysis. Persistent problems with leakage of coolant to the ambient made a redesign necessary. Another batch of PTAH-SOCAR ducts was manufactured (Figure 31-Figure 32). They were installed in a metallic jacket, and two successful test campaigns with nitrogen and kerosene as coolant were performed [24].

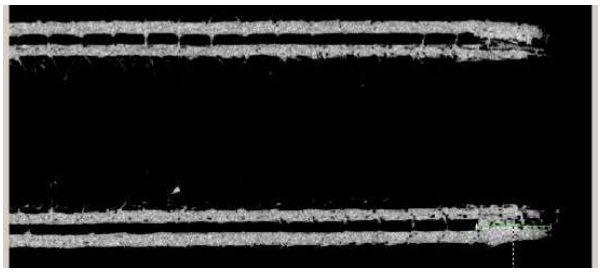

Figure 31: PSR-CMC segment manufacturing process: CT scan after R.CVI process

Figure 32: PSR-CMC liner machined for joining with the microfibre shells

Table 2 gives an overview over the number of firings with the different configurations and coolants.

Test specimen	PSR0	PSR1
Firings with GN2 coolant	6	9
Accumulated test time with GN2	117	205
Firings with Jet A-1 as coolant	4	5
Accumulated test time with Jet A-1	115	237
Overall accumulated test time	232	452

Table 2: Overview over test time and number of tests accumulated on PSR ducts

During steady state tests, no damage was detected on the hardware. In the last test, a dedicated test at elevated heat loads was performed, resulting in a defect on the oxidation protection coating, but leaving the CMC structure underneath intact. The test data recorded was analysed with respect to the pressure drop in the coolant channel, the influence of the coolant system pressure on the heat transfer to the fluid and the transpiration cooling effect through the porous medium. A comparison with prediction calculations showed good agreement between model and test data (Table 3).

duct	TEST	PC2 (bar)	O/F	PF2a (bar)	TF2a (K)	TF2c (K)	DTf	% DT	g/s	kW	Twall [K]	% on flux
PSR0	AEC-T10-07	9,1	2,2	42	277	Astrium/MBDA confidential		-20%	207	Astrium/MBDA confidential	1763	-18%
		9,1	2,2	42	277,2				207			
PSR1	AEC-T10-17	9,2	2,29	38,5	285,6			-8%	196		1663*	-11%
		9,2	2,29	38,5	285,6				196			
PSR0	AEC-T10-06	9	2,3	58,3	279,9			-21%	301		1591 *	-22%
		9,38	2,3	58,3	279,9				301			
h gaz 1 +20%		*9*	*2,3*	*58,3*	279,9			*-13%*	*301*		*1818*	
PSR1	AEC-T10-11	9,33	2,3	44,1	274,1			-12%	301		1589 *	-13%
		9,33	2,3	44,1	274,1				301			
PSR0	AEC-T11-01	18	1,8	61,4	276,5			-23%	342		1767	-24%
		18	1,8	61,4	276,5				342			
PSR1	AEC-T11-11	18,2	1,8	49,8	277,3			-19%	340		1766	-19%
		18,2	1,8	49,8	277,3				340			
											*	
nominal model (lst0)		**NANCY computations**							*8 W/m/K*		**no Si ? (<1683 K)**	
		experimental data										

Table 3: Comparison of test data with NANCY computations done by MBDA

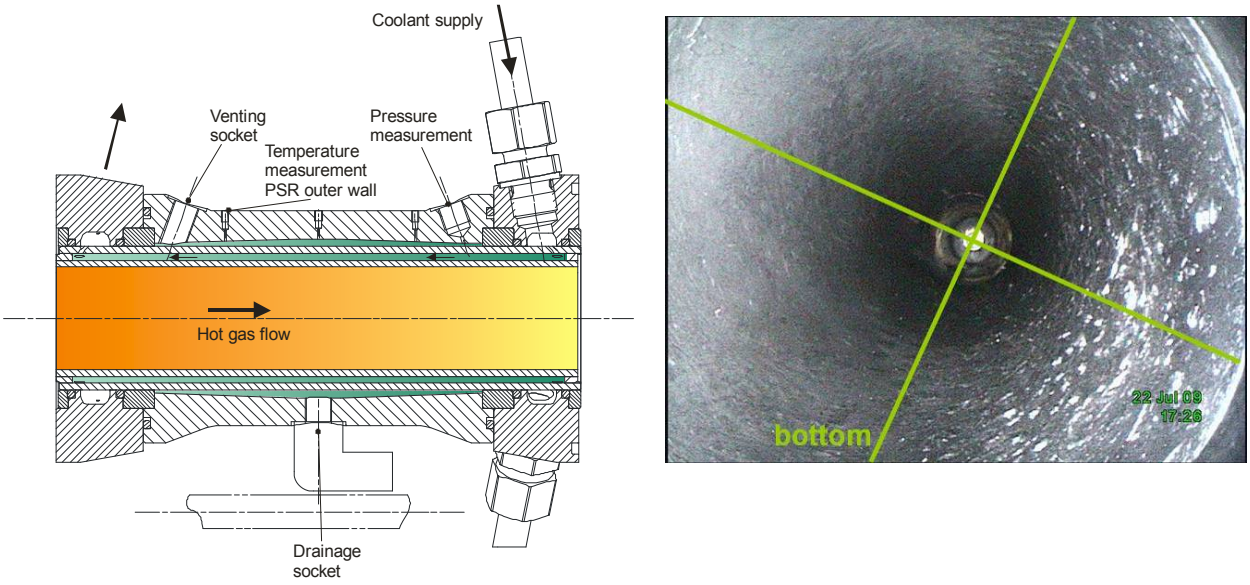

Figure 33: Experimental setup for convectively cooled CMC's at TUM (left), specimen after end of GN2 cooling test campaign (right)

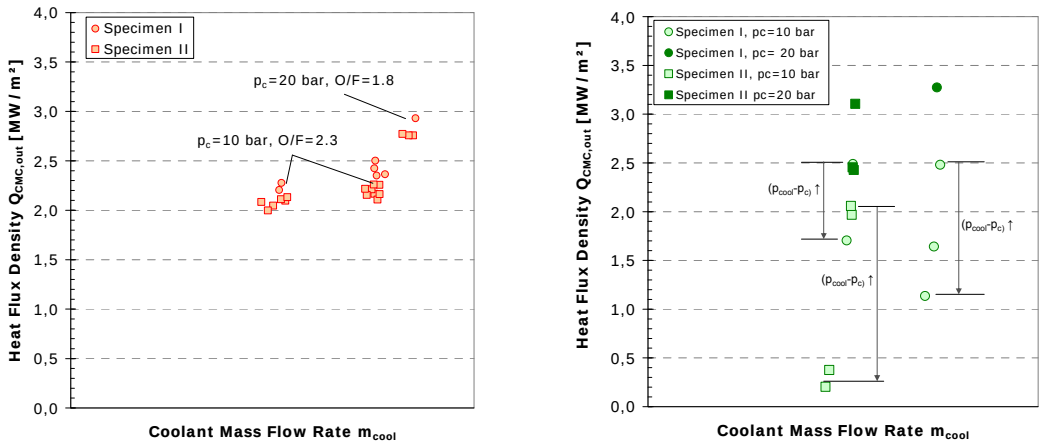

Figure 34: Heat fluxes recorded with nitrogen cooling (left) and kerosene cooling (right)

6.1.5 Metallic liners: oxidization process

Despite the large effort on CMC materials for combustor, the behaviour of some selected metallic materials is still of interest in a high-pressure oxidizing environment at high temperatures. After a material pre-selection by data / literature analysis was done, candidate materials for investigations were selected and a test plan for material property determination as well as material sample analysis was described. Physical property measurements (thermal conductivity, heat capacity, thermogravimetry under oxidative atmosphere) were performed. Different sets of samples were tested in an oxidizing atmosphere using a combustion chamber setup of Astrium on the TUM test bench (see *Figure 36* and *Figure 37*). Each sample was tested for an overall testing time of 300 s. In these tests, the stagnation temperature ranged from 800 K to 1050 K, depending on the mixture ratio. The chamber pressure was around 20 bar. Compared to airbreathing applications, the samples were subjected to much more severe conditions, as pure oxygen was used for the combustion, resulting in significant higher partial pressures of free oxygen at comparable pressure and temperature.

Post test analysis of several thermally loaded samples (visual, sample surface, oxide layer composition and thickness, microstructure, level of oxide layer formation, degradation, contamination, roughness, weight) were performed. After analysing the test results, three materials were chosen for tests with two different protective coatings each. Again, these six samples were tested in the ox-rich combustor at TUM. The post test analysis was used to assess the performance of the coatings in combination with the bulk material. The chemical analysis of the oxide layers on the different samples (e.g. Figure 38) was reflected against possible oxidation mechanisms.

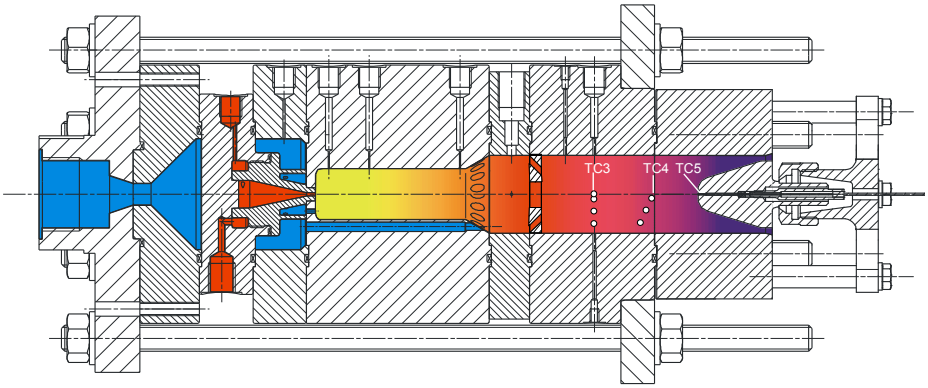

Figure 35: Cross sectional view of Ox-rich combustor (circles indicate location of hot gas temperature measurements)

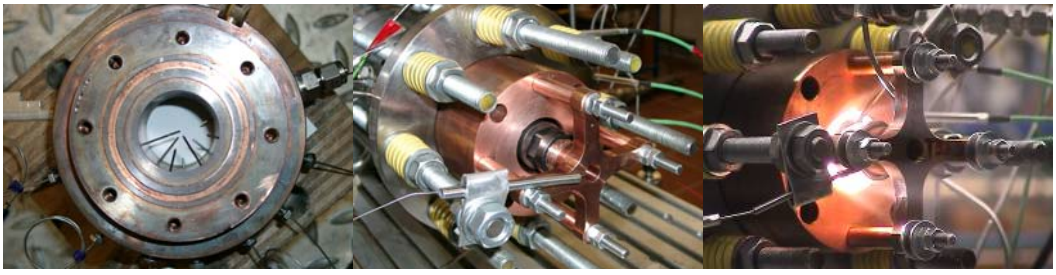

Figure 36: Ox-rich combustor setup

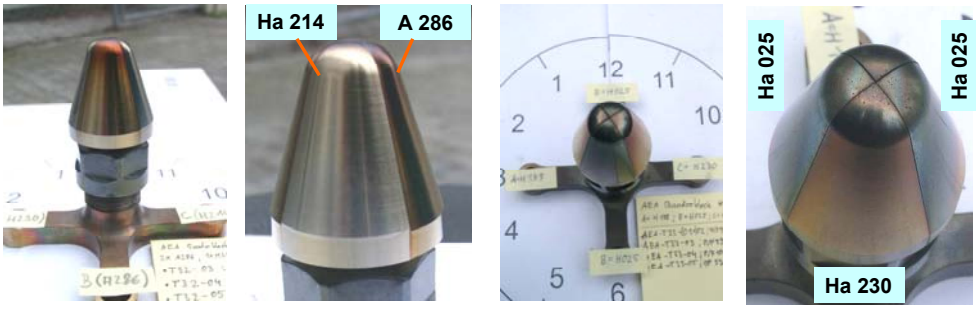

Figure 37: Hardware samples after test

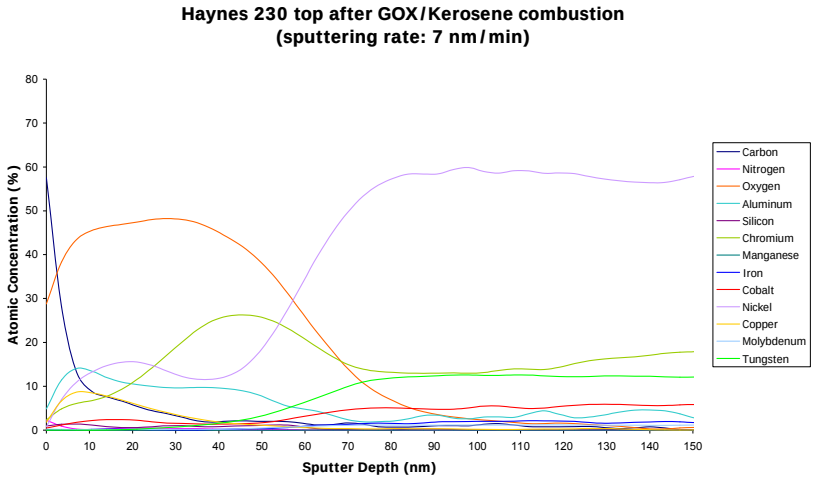

Figure 38: Haynes 230 composition: XPS depth profile at stagnation point after combustion

The analysis of test data using digital photography, surface profiling, XPS and EDX analyses led to the designation of Inconel 617 and/or platinum-coated Inconel 617 as the best candidate material for oxygen-rich combustion chambers to be employed in hypersonic aircrafts. The exceptional oxidation resistance of this alloy, lower cost and excellent mechanical properties were the guidelines for this material choice. A designation of the most performing between these two options was discussed as a function of production cost and lifetime of the combustion chamber under service. Further investigation is required for the indication of the best possible material choice among the two.

6.2 Cooling of Dual Mode Ramjet Combustors

At the ITLR facility for heated supersonic flow, experiments were carried out for different CMC materials [28], [29]. This facility is able to generate flows in the test section at a Mach number of 2.1 with total temperatures of up to 1450 K and total pressures of up to 10 bar. For this investigation, the highest temperature set was 1060 K and most of the experiments were carried out at a total pressure of 3 bar. During the project, a multitude of CMC samples were delivered: Carbotex^{SI} samples were delivered by ASTRIUM and charges of WHIPOX, OXIPOL and C/C by DLR. From every charge at least one sample was tested in the test channel. In total, 47 reference test cases with different samples at varying test conditions (subsonic and supersonic flow at medium and high temperature regime) were defined.

Figure 39 shows schematically the test setup: the test channel has a rectangular cross-section and has windows for optical access. A plenum containing the flat, porous samples is attached opposite to the window for IR-thermography. Within the samples, thermocouples were installed flush with the hot-gas surface. These were used for measuring the surface temperature and in situ-calibration of the infrared data.

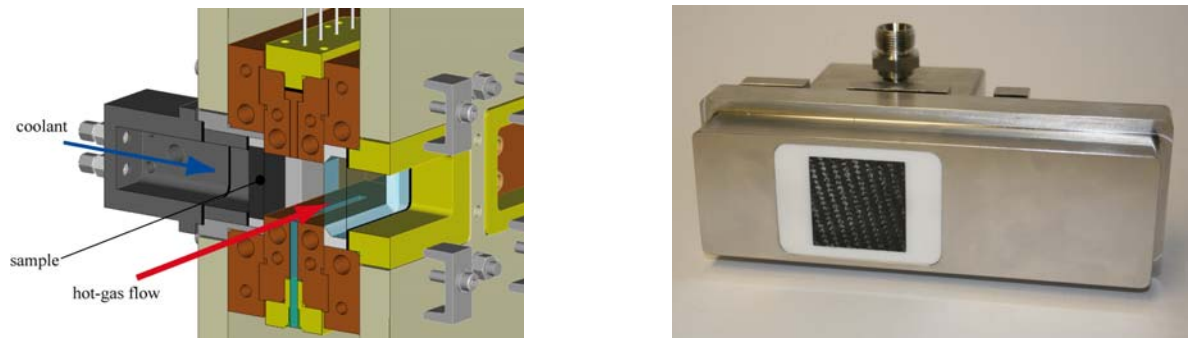

Figure 39: Sample-Integration Concept: Left: Hot-Gas Channel with Optical Access, Right: C/C Sample with Macor-Frame Integrated in Coolant Plenum.

6.2.1 Transpiration Cooling

In Figure 40, the 2D temperature maps of the surface of a randomly oriented C/C sample are shown. The flow is from left to right and at M=2.1 and at a total temperature of 1060 K. On top and bottom of the images the effects of the heat conduction from the sample into the water-cooled test channel can be seen. Due to this, the maximum measured surface temperature is not higher than ~670 K.

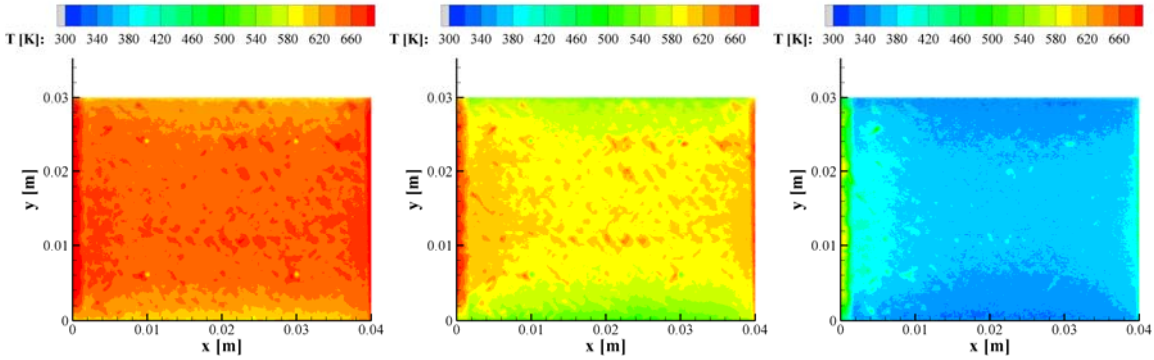

Figure 40: In Situ Calibrated IR Surface Temperature Distribution of C/C sample at Tt=1060 K. Left: F=0. Center: F=0.001. Right: F=0.01

Turning on the coolant (increasing blowing ratio *F*, which is the mass-flux ratio between the coolant exiting the sample and the main-flow) significantly decreases the surface temperature. For very high blowing ratios (*F*=0.01), the surface temperature almost reaches coolant temperature, which was injected from the back into the coolant plenum at ambient conditions.

The cooling efficiency Θ, a non-dimensional temperature ratio with respect to the wall temperature without blowing and the coolant temperature, is plotted versus the coolant mass-flow rate in Figure 41. A cooling efficiency of zero indicates the uncooled case, a value of unity complete cooling. For low coolant mass-flow rates, the cooling efficiency rises rapidly, whilst it turns somewhat asymptotic with higher values. Also, Figure 41 depicts the influence of the coolant on Θ: a coolant with a higher specific heat capacity yields also a higher cooling efficiency at the same coolant mass-flow rate.

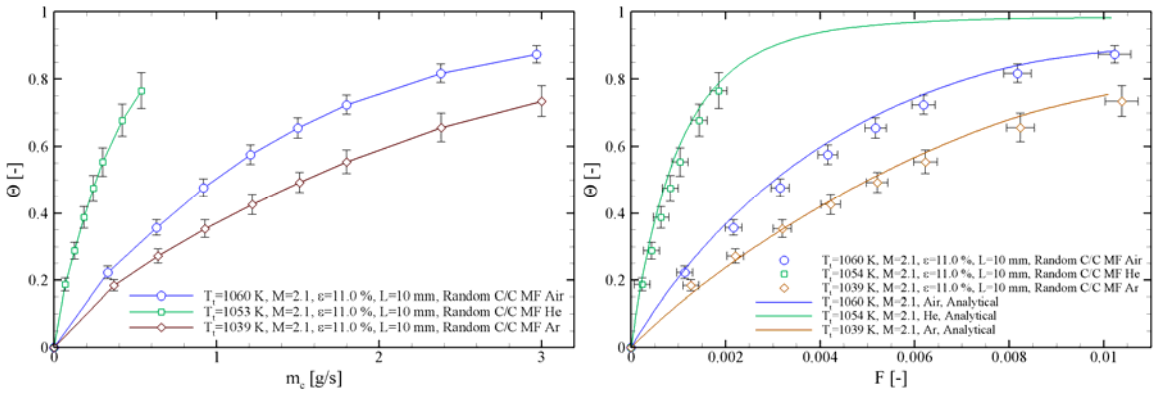

Figure 41: Random C/C Sample with Foreign Gas Injection. Left: Cooling Efficiency vs. Coolant Mass-Flow Rate. Right: Cooling Efficiency vs. Coolant Mass-Flow Rate Compared to Analytical Approach

An analytical 1D heat balance model was developed describing the cooling behaviour and coolant influence of the transpiratively cooled samples within the ITLR setup. It incorporates a model suggested by Kays et al. It is being compared to the experimental data in Figure 41 and shows a good agreement, meaning that the theoretical assumptions behind the transpiration cooling mechanisms can be applied to the investigated materials and coolants.

A manifold of tests have been carried out in a lower temperature regime of up to 500 K total temperature. To show that these data can also be extrapolated to higher temperature regimes, the cooling efficiency of the same sample (randomly oriented C/C) from different test campaigns and at total temperature levels has been compared to each other (Figure 42). One can see that within the margin of error, no difference in the non-dimensional temperature ratio Θ is apparent. This indicates that the definition of Θ is able to exclude the majority of erroneous effects, such as heat conduction, and to point out the transpiration cooling mechanisms.

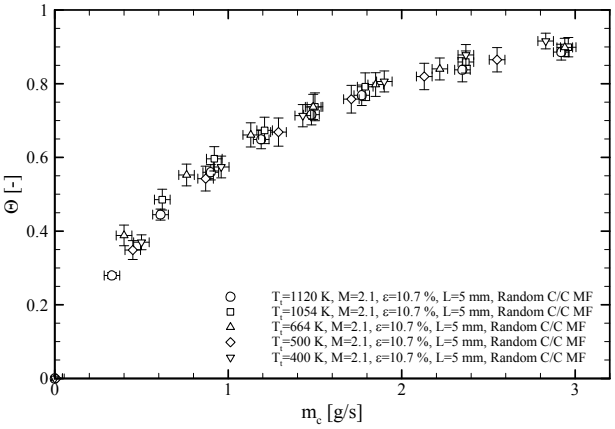

Figure 42: Random C/C Sample with At Different Total Temperatures: Cooling Efficiency over Coolant Mass-Flow Rate

When looking at the through-flow data in the hot-gas experiments, substantial differences between the different temperature levels (from cold, i.e. no main-flow, blowing against ambient up to $T_{t,g}$=1060 K) were observed (see Figure 43). Tests at a higher temperature level also led to higher pressure drops. This behaviour was attributed to the non-isothermal temperature profile within the porous wall. Locally, the density of the coolant is lower and therefore the local through-flow velocity is higher yielding a higher differential pressure drop. Furthermore, the dynamic viscosity changes, which leads to a higher pressure drop originating from viscous forces. First, a thermal equilibrium

was assumed within the sample between the wall and the coolant and a linear temperature distribution from coolant temperature up to the measured hot-gas surface temperature of the sample. These assumptions were implemented into the well established Darcy-Forchheimer-Equation, which leads to a modified version:

$$\frac{p_{in}^{\ 2} - p_{out}^{\ 2}}{2p_{in}L} = \frac{\mu_{in}}{K_D} v_{in} \frac{1}{\frac{b}{T_{in}}(n+2)} \left[(1 + \frac{b}{T_{in}})^{n+2} - 1 \right] + \frac{\rho_{in}}{K_F} v_{in}^{\ 2} (1 + \frac{b}{2T_{in}})$$

Where $b = T_w - T_{in}$ and the viscosity is temperature dependent following a power-law:

$$\mu = \mu_{in} \left(\frac{T}{T_{in}} \right)^n$$

In Figure 43 the experimentally obtained through-flow results are compared to the modified Darcy-Forchheimer equation for randomly oriented C/C at different thicknesses.

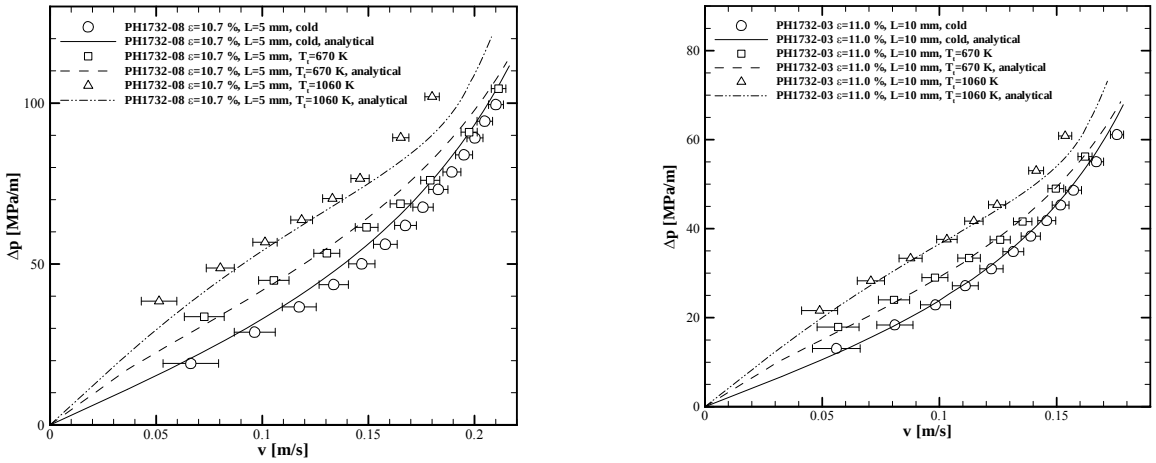

Figure 43: Pressure Drop vs. Through-Flow velocity in hot-gas tests: Comparison of Experimental Results with analytical model. Left: random C/C PH1732-08 L=5 mm. Right: random C/C PH1732-03 L=10 mm.

The normalized pressure drop has been plotted versus the though-flow velocity. With the given permeability coefficients the extended Darcy-Forchheimer model predicts the part sufficiently, where the deviation between the ambient through-flow test and the hot-gas test are the biggest, i.e. in the range of moderate blowing. This region is the most important for the technical application, because it is neither desired to reach full cooling of the wall, nor will it be possible to exceed the maximum bearable temperature of the wall material.

6.2.2 Regenerative Cooling

Additionally to the tests with porous CMC material, Carbotex^{SI} in PTAH-SOCAR design was tested in a cross-flow configuration, meaning that the coolant passes through the cooling channels and is not being transpired through the sample. This was done, because the permeability of this C/C-SiC material was extremely low. In Figure 44 the 2D-temperature data of the CarbotexSi in cross-flow configuration is being plotted. On the left hand side the surface temperature of the uncooled structure is shown. One can see the influence of the heat conduction due to the water cooled copper channel. A maximum surface temperature of approx. 710 K is being reached. Switching on the coolant naturally leads to a reduction in surface temperature of approx. 40 K (centre) for a blowing ratio of F=0.001

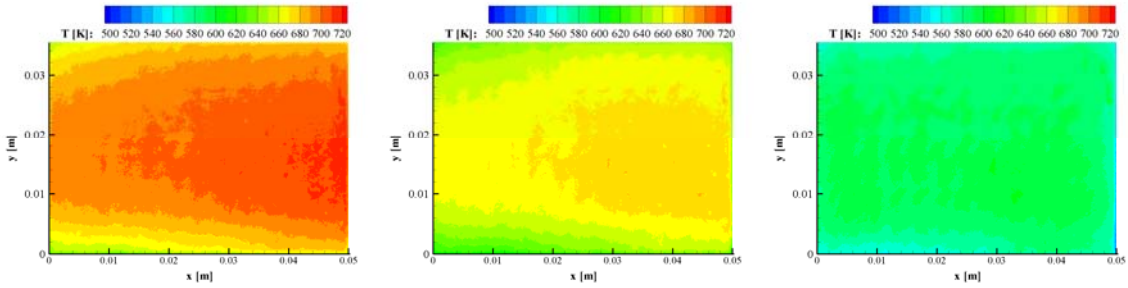

Figure 44: In Situ Calibrated IR Surface Temperature Distribution of CARBOTEX^{SI} CT1 sample at Tt=1057 K. left: F=0; center: F=0.001; right: F=0.015. Hot-gas glow direction from left to right.

In Figure 45 the cooling efficiency Θ of the samples' surface averaged temperature data has been plotted vs. the coolant mass-flow rate. First the increase is relatively strong, i.e. the coolant is able to remove a good amount of heat convectively out of the structure. This convective heat transfer within the sample reaches its maximum fairly quickly for higher blowing ratios, where the cooling efficiency curve becomes almost asymptotic at a value of 0.3.

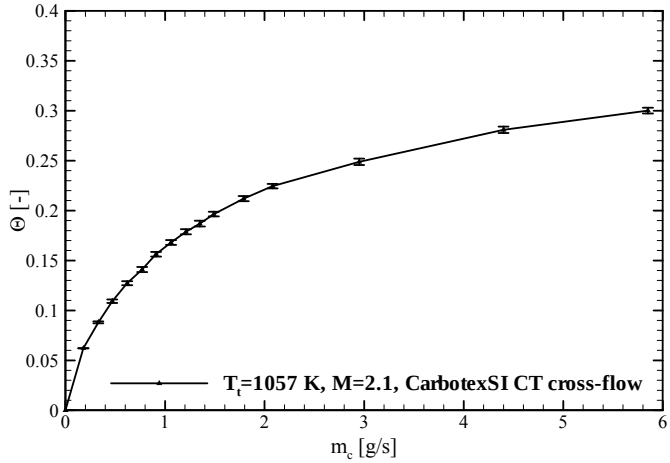

Figure 45: Cooing Efficiency of Carbotex^{SI} CT in cross-flow configuration

6.2.3 Effusion Cooling

An additional reference test case a multi-perforated plate was manufactured and tested similar to the CMCs. The in-situ calibrated temperature maps of the effusion cooled plate are shown in Figure 46. For the non-blowing case the typical cold regions for our setup at the top and bottom of the sample are shown. Theses regions are more dominant than for the CMC experiments due to the higher thermal conductivity of the plate material. This also affects the overall temperature of the sample. The maximum surface temperature at a hot-gas total temperature of $T_{t;g} = 500$ K is at around 410 K. The hot areas at leading and trailing edge can be attributed to residuals of the silicon sealing which has a different emissivity coefficient than the steel plate. Switching on the cooling decreases the surface temperature by a maximum of about 50 K. This maximum is reached rather quickly, since from a blowing ratio of $F = 1{:}0$ up to the maximum tested blowing ratio of $F = 1{:}45$ the difference in the 2D-maps are almost not visible anymore. The cooling efficiency Θ for the multi-perforated plate has been plotted vs. the coolant mass-flow rate in Figure 47. It shows the values for the surface thermocouples. The same behaviour as for the temperature maps of Figure 46 can be observed.

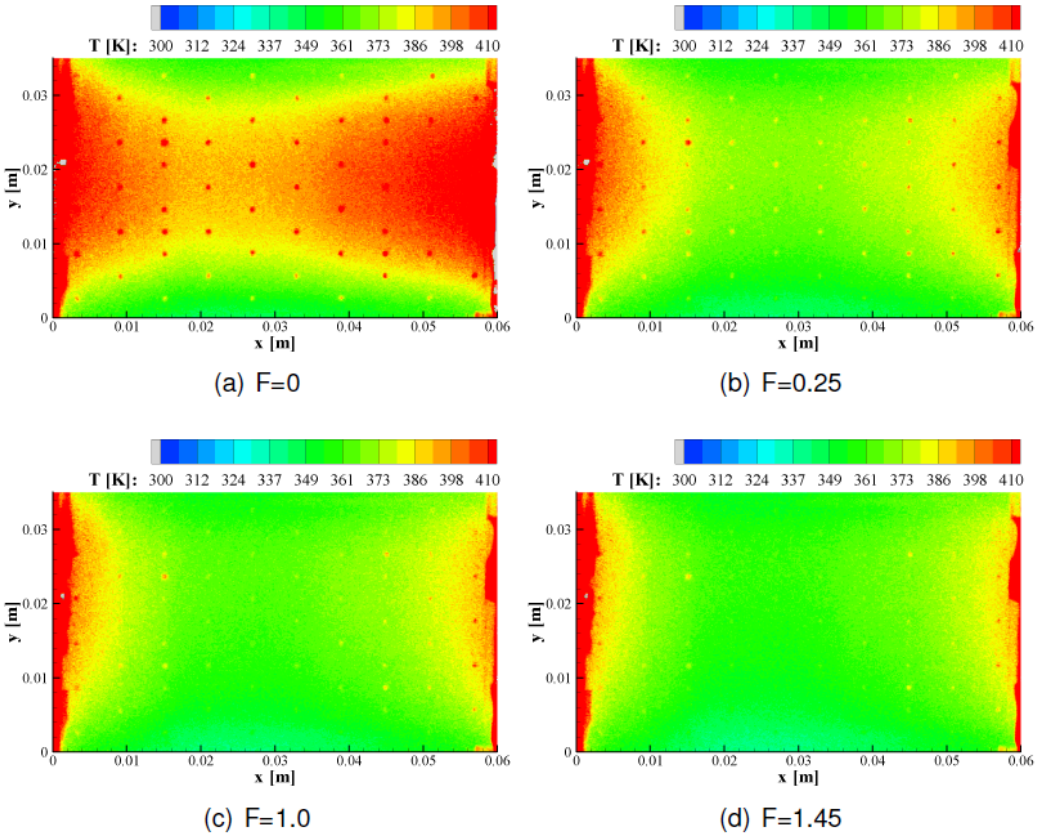

Figure 46: Surface Temperature Distribution of the Effusion Cooled Multi-Perforated Plate at M = 2:1 and Tt;g = 500 K (flow from left to right)

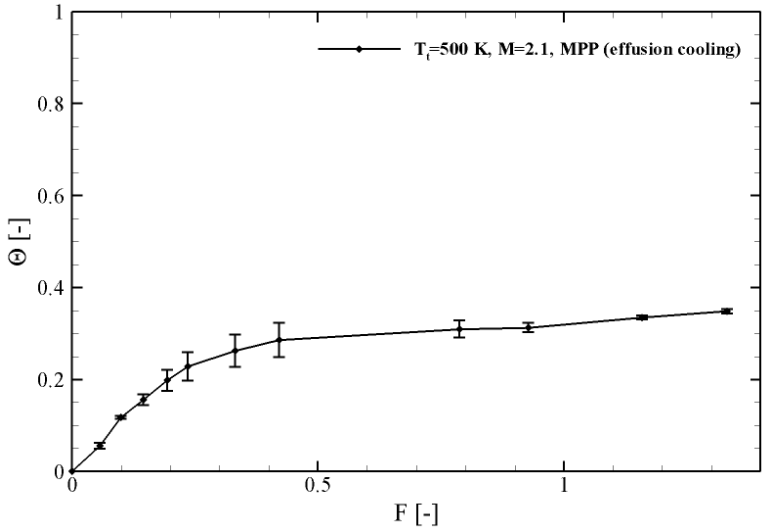

Figure 47: Cooling Efficiency of the Multiperforated Plate (MPP)

6.2.4 Relative comparison of different cooling techniques

For thermal management design practice, the efficiency of the different cooling techniques is of great importance. A good know-how of the cooling efficiency Θ allows the thermal designer to assess whether a certain technique is preferred above another. Having the efficiencies of the different techniques plotted on the same Figure 48, indicates clearly that only transpiration cooling can assure a low wall temperature for a thermally loaded liner, even with relative low transpiration

mass flows. In case where fuel is used as coolant, the related amount of fuel mass flow injected as transpired coolant might not always advisable from a thermodynamic point of view (cycle efficiency). In that case, it might be better that one goes for a larger mass flow rate of fuel (coolant) which will pick up regeneratively, i.e. convectively, the combustor heat at the wall and inject the heated up fuel into the combustor at a proper location. The application of transpiration cooling can then be allotted to these structures or locations where convective cooling is insufficient, e.g. struts, fins, separation and reattachment locations…

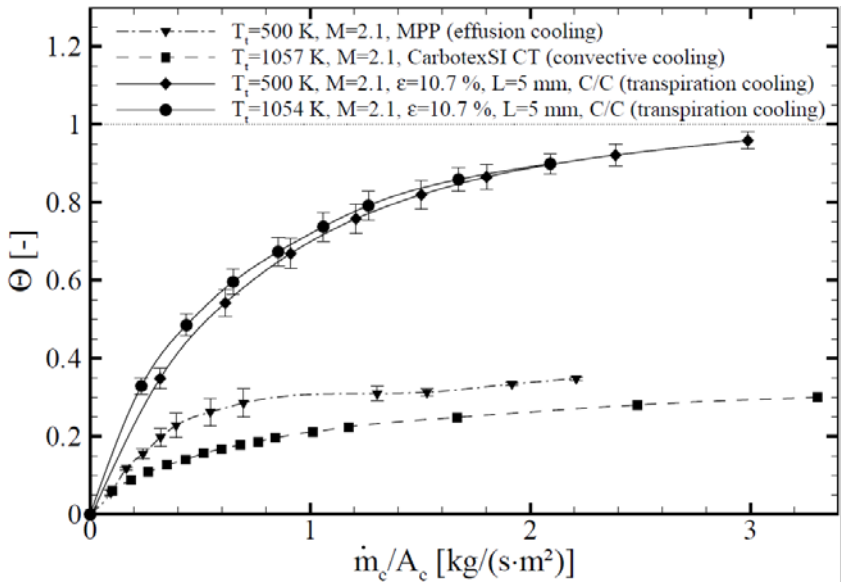

Figure 48: Relative comparison of cooling efficiencies for effusion, transpiration and convective cooling

6.3 NOx emissions

Finally, a detailed study was performed to predict NOx emissions of the two different reference vehicle configurations during take-off and cruise flight. Whereas the emission levels for the Mach 3 vehicle seem to be within the emission limits foreseen for future air transport, the Mach 6 vehicle, due to the high combustor inlet temperature, is expected to produce NOx emissions significantly above any conceivable future limit (see Figure 49).

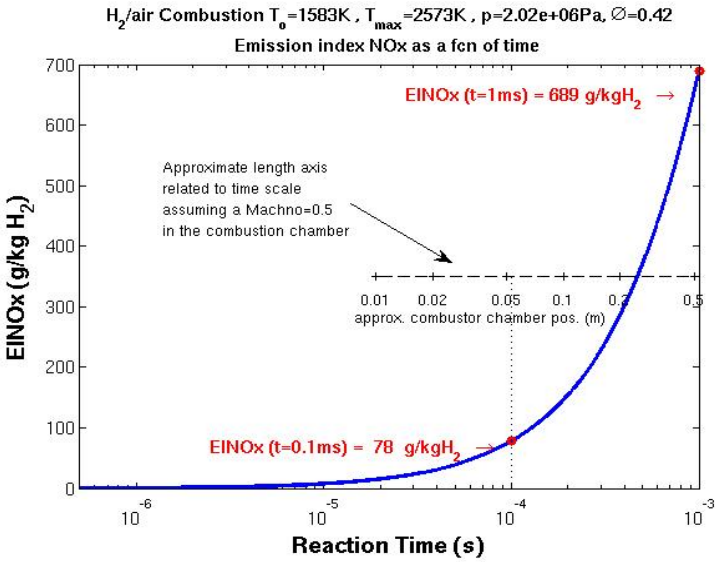

Figure 49: Baseline EINOx development equivalence ratio ∅=0.42H2 combustion for Mach 6 vehicle

Therefore, different countermeasures were investigated with respect to their applicability and effectiveness. Possible “low-NOx” concepts studied, RQL, water injection and the more drastic N2-O2 separation, showed only limited and insufficient NOx reduction starting out from baseline conditions. Based on these ATLLAS studies, either new technology findings that could facilitate combustor residential times of the order of some tenths of milliseconds need to appear, or a re-design that allows for very low equivalence ratios typically of the order 0.25, resulting in combustion chamber temperatures around 2250K, is needed.

7. Material-Aero-Thermal Interaction Modelling

In parallel to the above described experimental investigations, the modelling aims at enhancing and testing the coupled aero-thermal phenomena in the ATLLAS type high speed flows. The phenomena studied are shown in Figure 50 and described in more detail in [30] below. They addressed different approaches (CFD, semi-empirical, commercial or in-house codes …). Comparisons have been performed with analytical and experimental results from literature, and some numerical cross-checks are planned.

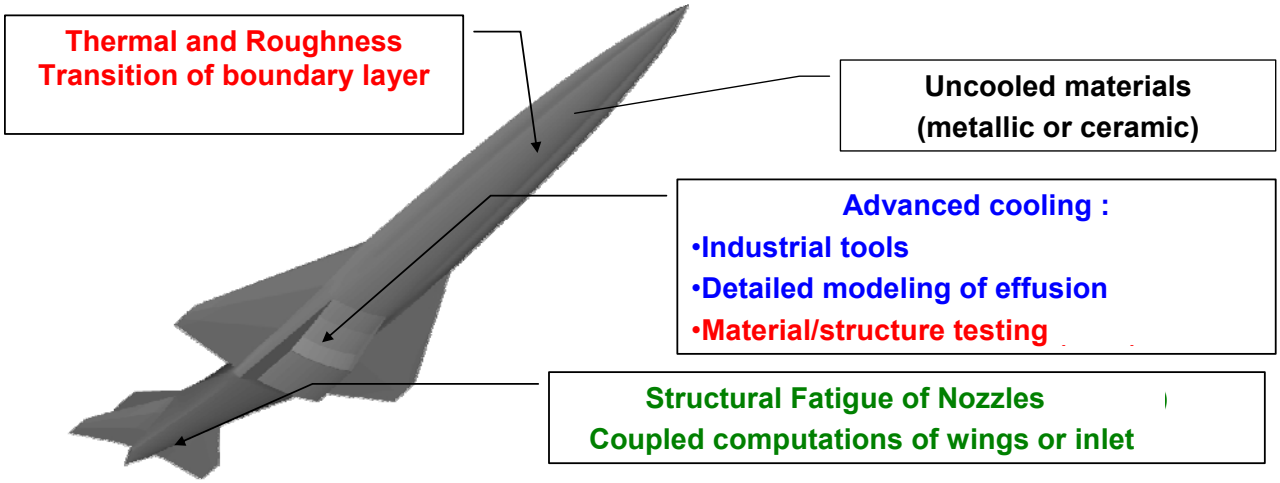

Figure 50: Investigation of coupled phenomena on Mach 6 generic aircraft

The emphasis in the area of loads definition is to develop and verify models to predict the combined effect of aero-thermal and material interaction on several lightweight high-temperature resistant materials. This is accomplished by integrating existing aerodynamic, heat-transfer, and structural codes. The results are then calibrated and verified with simplified experiments. The generic high speed aircrafts is a support for the requirements of both the coupled phenomenon computational tools and the experimental works: TUM for high pressure combustor for turbojets and ITLR for ramjet based combustors related to cooling techniques or advanced materials investigation.

The TUM combustion experiment was computed with different approaches. MBDA computed in 3D with CFD-ACE while ASTRIUM did some 2D with its empirically tuned code ROCFLAM (Figure 51). Comparison made on heat fluxes on the different segments of the water-cooled calibration chamber gave correct agreement with experiment, except in the first segment, where mixing and ignition takes place.

ESTEC and MBDA focused on the modelling of multi-physics flow phenomena within porous media. On the basis of the commonly-stated computational plan, several porous medium and combustion test cases have been computed with different levels of refinement. As the test cases are completed, the software porous media flow-through model implementations are validated versus the different experimental campaigns.

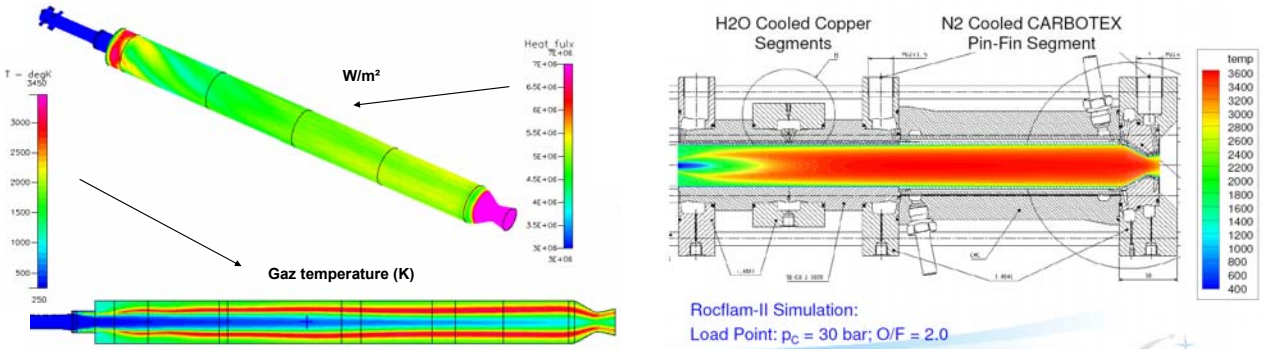

Figure 51: NS computations of TUM experiment (left: 3D MBDA with CFDACE; right: 2D ASTRIUM with ROCFLAM)

For the heat transfer in porous media, a basic experiment was chosen in the published literature. The work of Provence University in Marseille consists of a porous medium (either glass or bronze), heated on two sides and fed with cold liquid pentane. The numerical sketch is given on Figure 52.

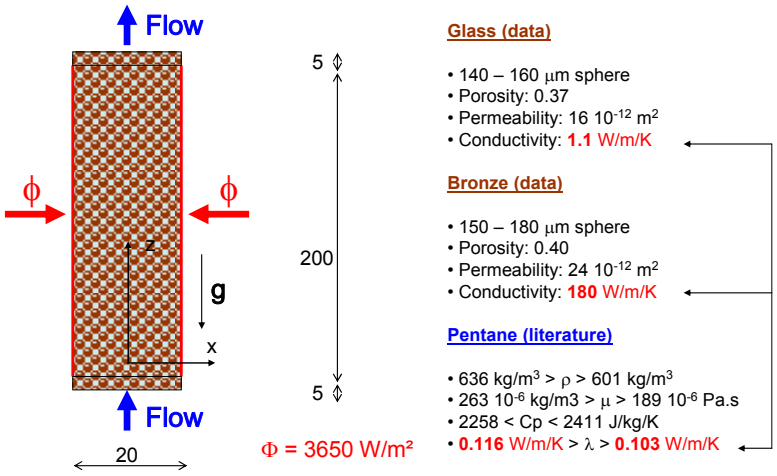

Figure 52: Basic test case of heat transfer in porous media from Marseille laboratory (Rahli et alii)

Different computations are performed by MBDA on the two experiments while varying the way of computation of the porous medium equivalent conductivity, from serial to parallel assumptions. The default formula used by CFD-ACE and the serial formulation give temperatures close to the measured ones for the glass sample.

The ITLR supersonic test case is the final check for the validation process done for air at three total temperatures: $T_{t,g}$ = 450 K, 600K and 1060 K [27] [28] [29] [31] [32]. The wall temperature has been plotted versus the streamwise sample length for the lower value of $T_{t,g}$ = 450 K and the highest value of 1060 K (Figure 53). The thermocouple readings are shown as cross symbols in the plot. The numerical values have been extracted at the interface between the porous zone and the main-flow zone. The recovery temperature of the hot-gas is not reached in any data point of the plot, due to the non-adiabatic setup. A wall temperature profile was imposed down and upstream of the sample, obtained by a thermal analysis. The sensitivity of the temperature at the interface between the porous medium and the main flow is relatively high with respect to the thermal boundary conditions set at the side-walls of the sample.

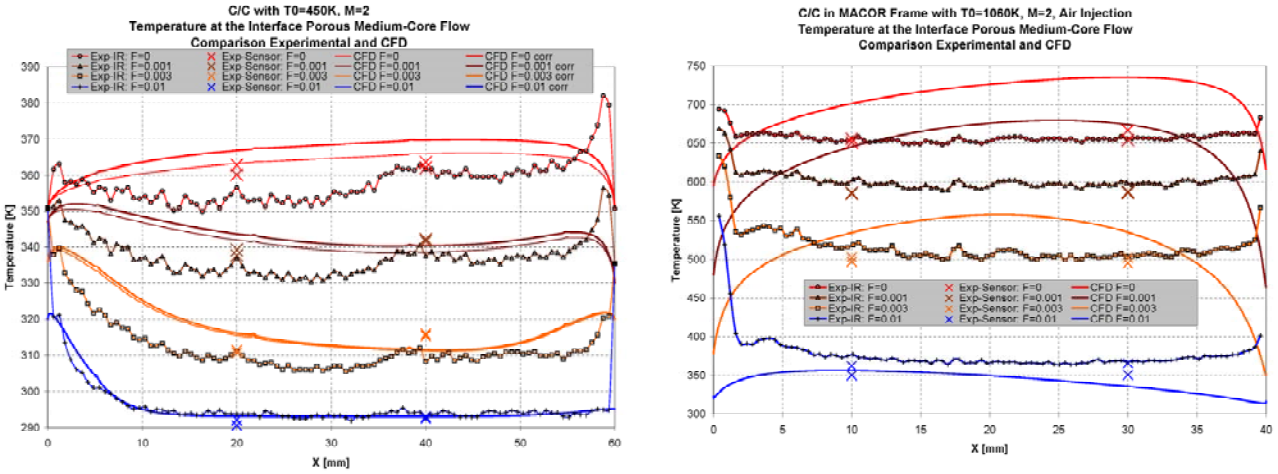

Figure 53: Comparison between experimental and numerical results: temperature at the interface for different blowing ratios and core flow total temperatures: left: $T_{t,g}$ = 450 K; right $T_{t,g}$ = 1060 K.

For $T_{t,g}$ = 450 K, the agreement between experiments and simulations is very good (Figure 53). For $T_{t,g}$ = 1060 K, the agreement between experiments and simulations is only good for the high blowing ratios. A discrepancy can be seen for the lower blowing ratio cases. This difference in computed and experimental interface temperatures increasing with freestream total temperatures was found to be due to thermal losses not taken into account in the CFD, i.e. radiation and translateral heat conduction. Based on a reduced heat balance model, the calculated extra heat losses are nearly 30% higher than the convective or the perpendicular conductive heat transfer for the test case at 1060K. Radiation is limited however and is only accountable for 10% of the additional heat losses. For higher blowing ratios, the agreement between the experimental data and the numerical temperature distribution is very good. The cooling effects, i.e. heat flux reduction and internal heat exchange, are dominating the thermal behaviour.

In Figure 54 the cooling efficiency is being plotted over the blowing ratio for $T_{t,g}$ = 450 K, 600K and 1060 K both for the experimental and numerical values. The general trend of the cooling efficiency, i.e. the relative surface temperature reduction with respect to the no blowing case can be reproduced very well by the numerical model.

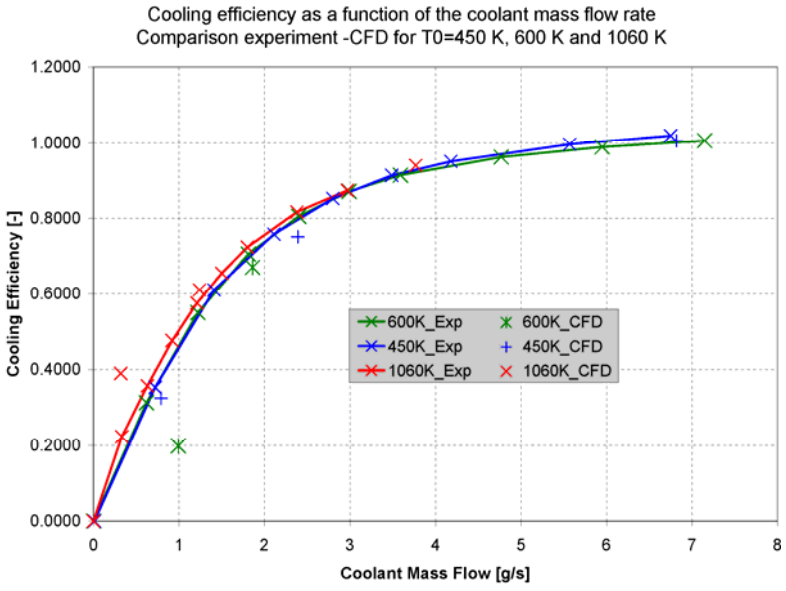

Figure 54: Numerical and experimental cooling efficiency vs. blowing ratio for $T_{t,g}$ = 450 K, 600K and 1060 K.

The final goal however is to use the hydrogen fuel rather than air as a coolant for the combustor walls. Therefore in a first step helium was used during experiments to get closer to the thermal capacities of hydrogen but yet avoiding interaction of combustion induced heat transfer. For the simulation, the extension towards hydrogen with and without combustion was performed to assess its global effect. In Figure 55, the density is plotted for the highest blowing ratio. Due to the helium transpiration, a shock wave is generated at the upstream side of the porous medium being reflected at the top wall.

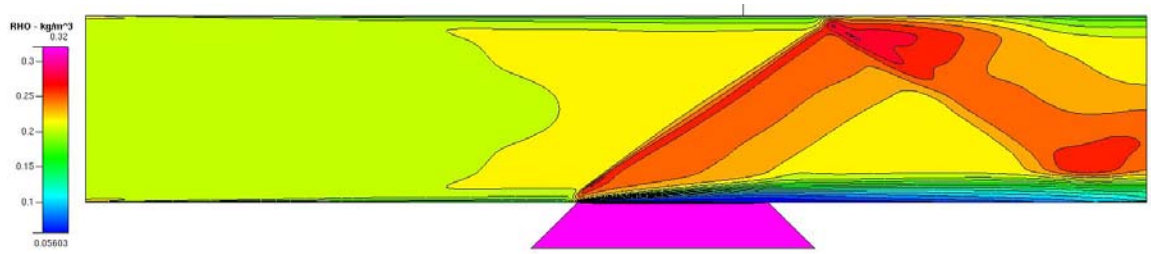

Figure 55: Helium coolant injection: density contours.

In Figure 56, the experimental results shows the cooling efficiency obtained with transpiration cooling with air (blue) and helium (green). The simulation results are added for the lowest, intermediate and highest mass flows of coolant. The results obtained for Helium are in very good agreement with the experimental results. Predictions of cooling efficiency obtained with hydrogen are represented in red. Due to the reduced mass flow, using the hydrogen fuel as transpiration coolant is of interest for high-speed engines.

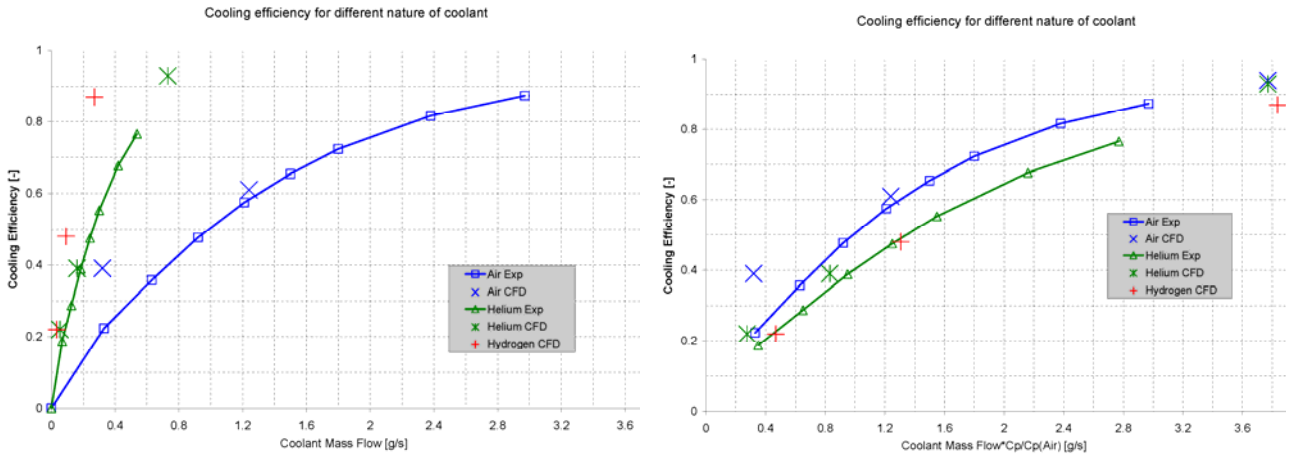

Figure 56: Cooling efficiency as a function of coolant mass flow and coolant mass flowC_p/ C_p(Air).for Air, Helium and Hydrogen.*

Plotting the cooling efficiency in function of a relative mass flow rate with respect to the heat capacities as shown in Figure 56, clearly demonstrates the similarity parameter to be used for design purposes.

To examine how the hydrogen film reacts with the core flow, several combustion simulations have been performed where hydrogen is used as a coolant. In figure Figure 57 the mass fraction of OH is plotted on the same scale, from 0 to 0.008. The blowing ratio is increasing from top to bottom. For the lowest value F=0.00032, the combustion is attached to the porous interface. When the blowing ratio is increased to 0.00073 (case 2), the ignition is delayed due to the increased cooling

effect of the H2 transpiration. For F=0.00098 (case3), the combustion is even more delayed as temperature drops to lower than 900K. However an oblique shock induced by the transpiration cooling starts to become more prominent resulting in a higher core temperature above the porous sample (Figure 58). Increasing the blowing ratio to F=0.0013 (case 4), the oblique shock is stronger resulting in a higher heat flux towards the wall. This results in an increase of the wall temperature (> 1000 K) despite the higher cooling capacity of the transpiration. The combustion ignition location moved upstream accordingly to the reflected shock wave location. For F=0.0015 (case 5), the oblique shock wave angle is maximum and the ignition location goes slightly upstream despite the increased cooling. Again, a balance is settling between oblique shock and cooling conditions. The impact point of the reflected oblique shock wave is a preferred location due to the increase of temperature. For F=0.0018 (case 6), the location of the ignition does not vary as the shock wave angle remains almost constant. Nevertheless, the combustion becomes unsteady for the largest blowing ratio.

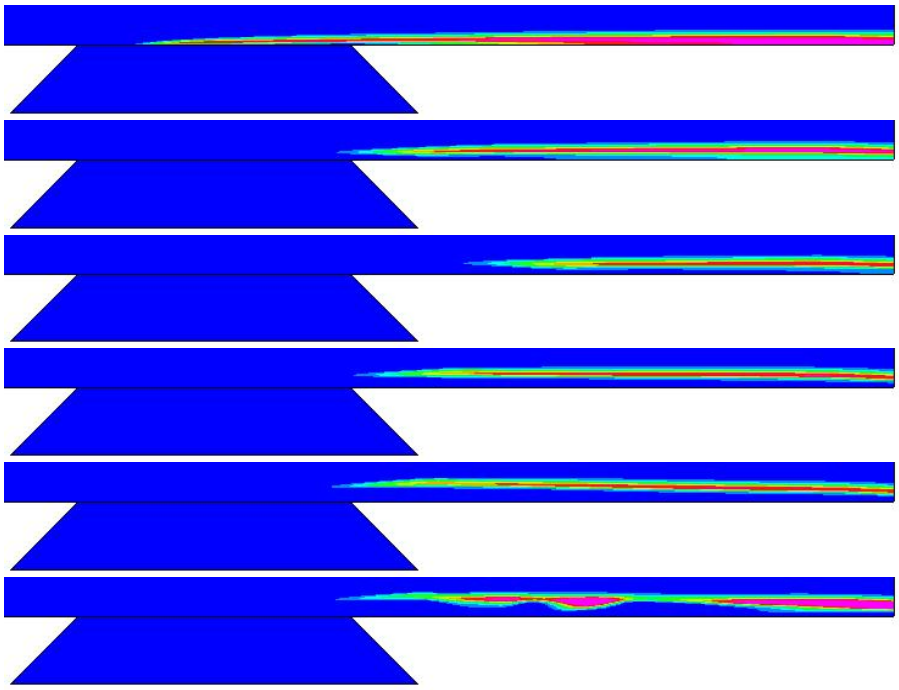

Figure 57: Ignition location as a function of increasing blowing ratio: from top to the bottom, case 1 to case 6.

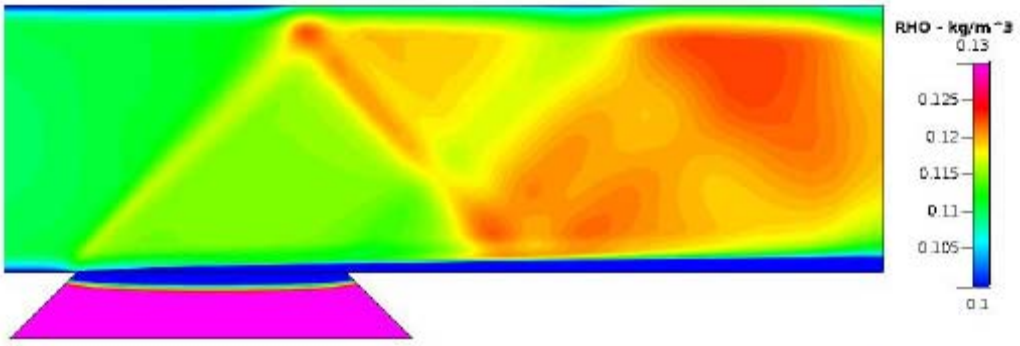

Figure 58: Combustion ignition location related to reflected shock wave: case 6 (density contours).

In Figure 59, the skin friction is normalized with the no-blowing case. The skin friction decreases clearly with blowing ratio and becomes negative once the presence of the oblique shock wave is prominent. This decrease in skin friction is not limited above the porous plate but persists further downstream. Apart from lower wall temperatures, the related reduction of skin friction has an additional advantage in decreasing the viscous drag in the combustor as well.

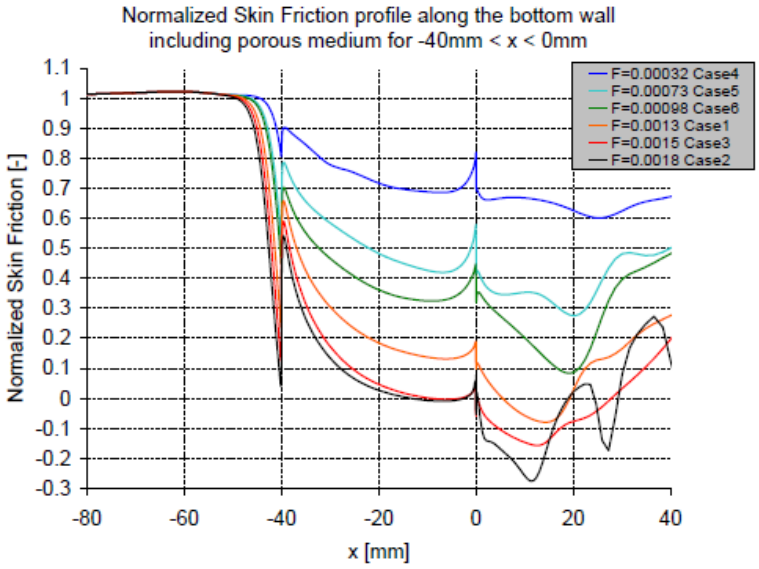

Figure 59: Normalized Skin friction

Whereas transpiration cooling clearly has a much better efficiency, due to the direct contact between the coolant and the solid wall to be cooled, this is less evident for effusion cooling. Detailed effusion cooling computations were performed at ONERA by means of an in-house CEDRE CFD tool on an experimental test case from Texas University. It entails a full geometry (10 half holes arranged in a staggered manner) with 2 blowing ratios (blowing ratio 0.25 and 0.65) and 2 main flow turbulence intensity levels (18% and 0.5%) After more deep investigation of the quasi periodic limits as well as the effect of refinement of the mesh, a new parametric study corresponding to an actual geometry tested at ITLR is made. The example of Figure 60 gives temperatures along the plate with an A310 (NS30) high temperature alloy extensively used by MBDA for hypersonic propulsion metallic structures. Agreement was good between experiments and computations.

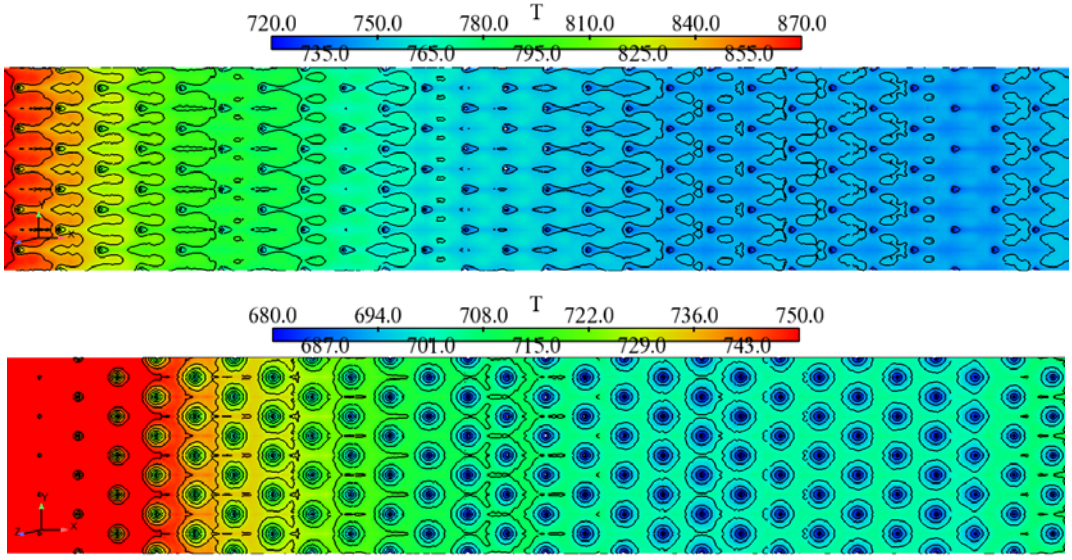

Figure 60: Hot and cold temperature maps of the metallic multi-perforated plate in ITLR hot flow conditions

A numeric aero-thermo-elastic analysis tool has been developed by FOI. It allows an accurate prediction of the coupling among the flow-field and structural components, highlighting the mutual interactions among heat transfer, aerodynamic loads and structural dynamic response. One of the main purposes of such investigation is the analysis of the structural integrity due to high temperatures and dynamic loads for the design of nozzles and thermal structures in high-speed

flight applications. The proposed methodology is demonstrated on a typical panel in the nozzle part of the ATLLAS generic aircraft. This part of the aircraft is challenging, from an engineering point of view, as it is heavily loaded not only by local pressures and thermal loads but also by global forces acting on the rear part the aircraft. The panel is heavily heated on one side by the hot exhaust gases and at the same time cooled on the back side by the liquid hydrogen tanks inside the aircraft. This result in large temperature gradients through the thickness and creates potential problems with large thermal stresses and strains in the structure, that need to be accounted for in the thermal design. A coupled simulation performed for Mach 6 conditions of aerodynamic pressure, is shown in Figure 61. Different combinations of cooled or non-cooled lightweight sandwich structures with and without load carrying capability have been investigated.

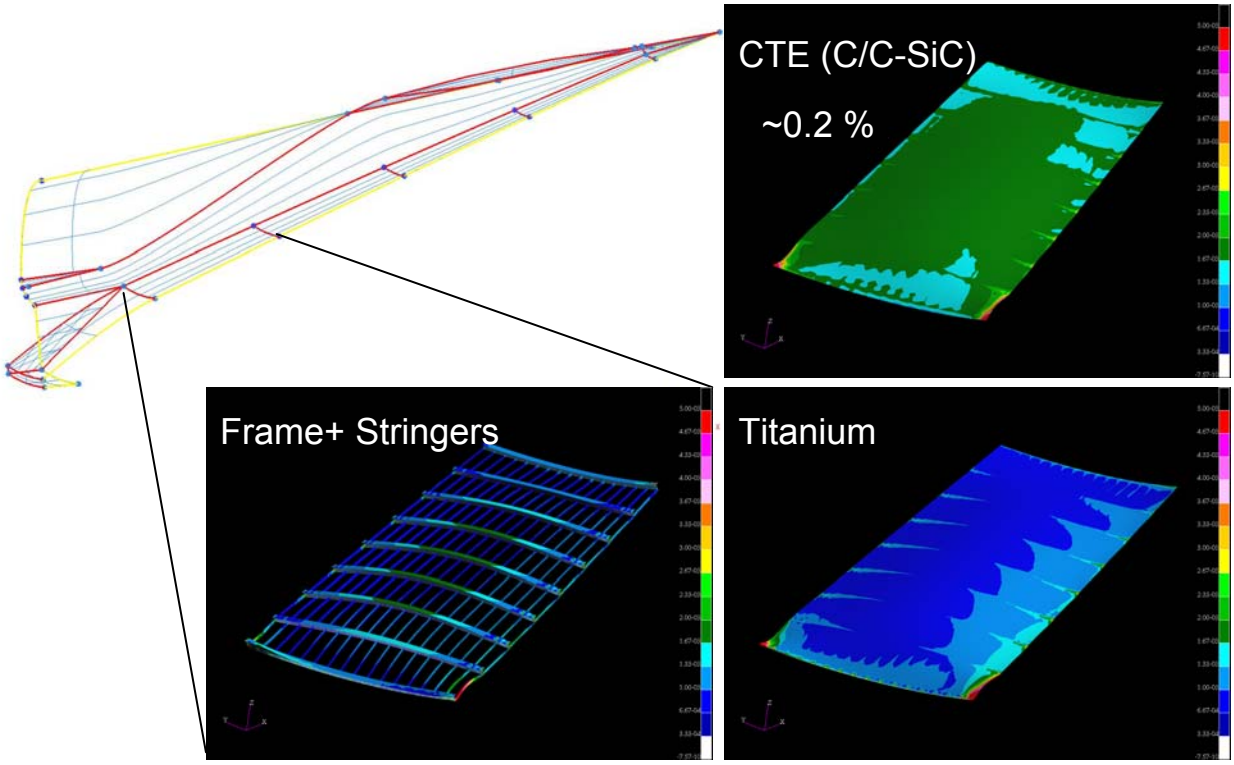

Figure 61: Aerothermal loading of a nozzle sandwich panel with a Ti-sheet on the cold side and C/C-SiC on the hot side

The aero-thermal heat loads for intakes are somehow more difficult to assess than nozzles as they are prone to transition. Due to the compressibility and cold wall temperatures, the transition process is delayed and experiences a larger extent than what one would expect from incompressible theory. However, there is hardly any information available about the combined effects of compressibility, hot walls and roughness. Therefore a combined experimental and numerical effort is carried out to gain a thorough understanding of the physical processes taking place.

As an example, Figure 62 illustrates a breakdown process towards a turbulent spot induced by a roughness. Depending on the roughness height, the induced hairpin vortices can degenerate or amplify resulting finally into a classical breakdown process. The presence of turbulence is confirmed by the familiar hairpin structures that are to be found in the centre of the spot. This process can somehow be confirmed by experiments though the DNS results allows one to better understand the sequential physical processes taking place. The final results allow providing some correlations for transition onset and extent for the above application as shown in Figure 63. The

cold wall reduces the spread angle of the turbulent spot by 20 to 30%. The lower wall temperature reduces the sound speed within the boundary layer (increasing the local Mach number), so it is perhaps not surprising that the reduced wall temperature has a similar effect to an increased Mach number on spot growth rate [35].

Performance of the transition experiment at Mach 3 and 6 with turbulent spot detection is investigated experimentally at ALTA (Figure 62) [34]. A variable roughness height allows deriving easily the critical Reynolds number at which the breakdown is triggered. A comparative analysis with the DNS data is indicated a good mutual correspondence as shown in Figure 63.

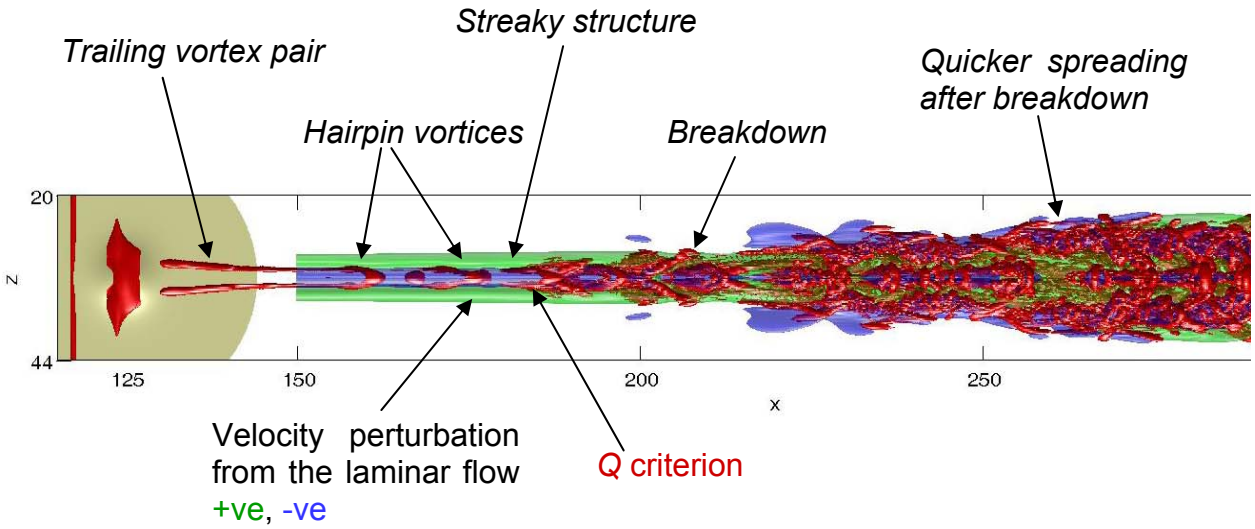

Figure 62: Typical breakdown process within a compressible laminar boundary layer downstream of roughness.

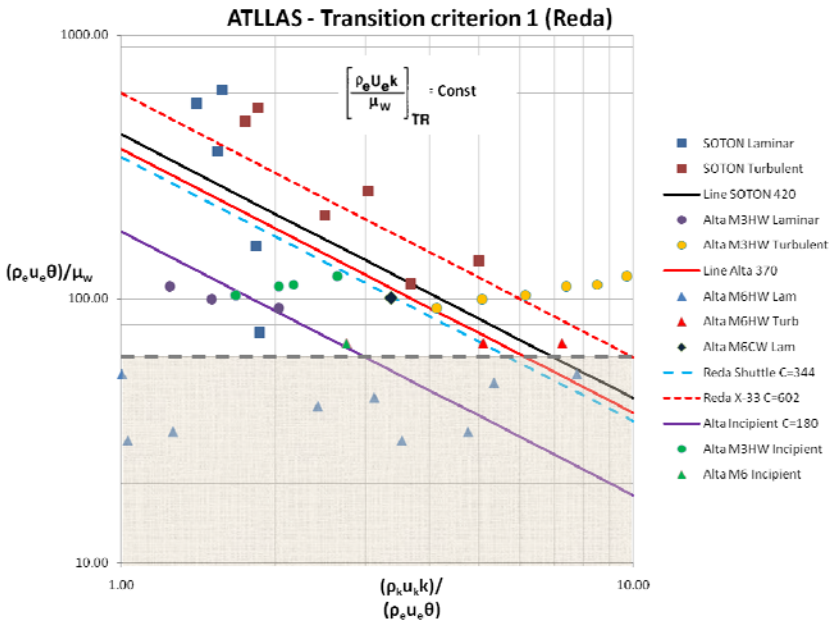

Figure 63 : Effect of roughness on transition: ATLLAS experimental and numerical results compared with a proposed transition criterion compared to other available criteria.

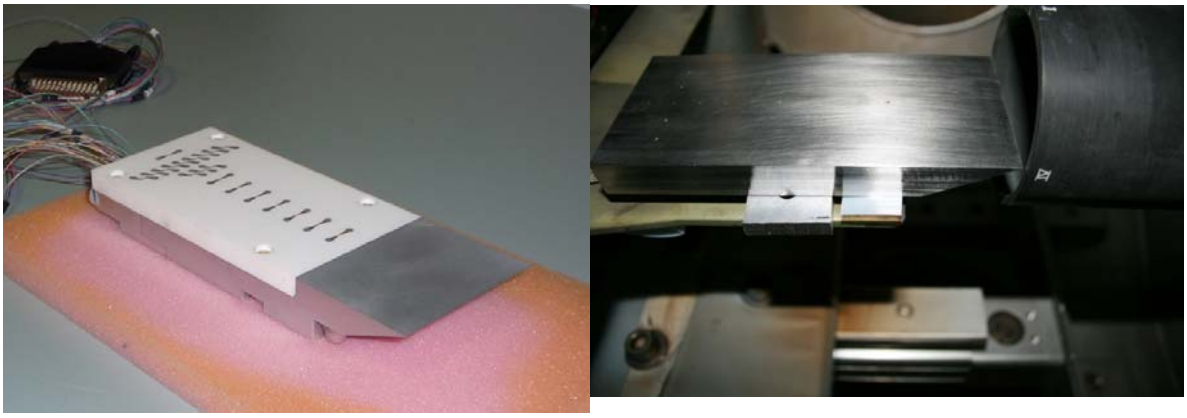

Figure 64: Hot film gauged model with instrumentation detail (left) and thermocouple equipped flat plate in front of the HEAT Mach 6 nozzle (right)

8. Conclusions

It is quite clear that a lot of technologies need to be brought to a higher technology readiness level before one can even envisage kicking-off the manufacturing and operation of these types of vehicles. However, it is important that first the know-how and experience is put in place to assess whether or not any sort of high-speed concept has the required cruise performance. The study has shown that a cruise efficiency above three, i.e. L/D ratio times the propulsion efficiency, is recommendable for a long-haul cruiser. This can be achieved with the newly designed kerosene based Mach 3.5 vehicle M3T which is also well above the Concorde's figure of merit. With a 300tons gross take-off weight, the 200 passenger vehicle achieves a range beyond 10,000km (5,500NM) after a 150ton fuel burn. The hydrogen powered Mach 6 vehicle is however rather disappointing even after a dedicated optimization process. With a GTOW of 278tons including the 110tons of hydrogen fuel, the 200 passenger vehicle's range could be brought up with 10 to 20% to 7,400km (4,000NM) which is still below the envisaged 9,000km. This doesn't mean a Mach 6 is intrinsically not conceivable, but indicates rather that a 'classical' design as proposed by Lockheed is not recommendable and should be avoided. A different architectural design or an improved engine design, including intake and nozzle, is needed to make it attractive. This perspective is not out of scope as a Mach 5 A2 vehicle conceived during the LAPCAT project can achieve this critical cruise efficiency. The better performance for the latter is mainly due to a well designed engine concept.

Overall design methods for high-speed transports at Mach 3 and 6 are revisited to increase the lift/drag ratio and volumetric efficiency through respectively a dedicated conceptual design methodology and a MDO-process. Within this MDO process, the need of lightweight and heat resistant materials is a prerequisite for a successful design.

Therefore, the prime focus of the ATLLAS project was on assessment of materials, cooling techniques and their interaction with the aero-thermal loads for both the airframe and propulsion components. The former focuses on sharp leading edges, intakes and skin materials coping with different aerothermal loads, the latter on combustion chamber liners. After material characterisation and shape definition at specific aero-thermal loadings, dedicated on-ground experiments are conducted. Both Ceramic Matrix Composites (CMC) and heat resistant metals are tested to evaluate their thermal and oxidiser resistance. In parallel novel cooling techniques based on transpiration and electro-aerodynamics principles are investigated.

Combined aero-thermal experiments tested various materials samples with a realistic shape at extreme aero-thermal conditions for elevated flight Mach numbers. Dedicated combustion experiments on CMC combustion chambers allow the reduction of combustion liner cooling resulting into overall thermal efficiency increase. Particular aero-thermal-material interaction influences strongly the aerothermal loadings. Therefore conjugate heat transfer, transpiration cooling and compressible transition phenomena are investigated and modelled. Similarly, the interaction of hot walls on high-speed transition is of utmost importance for intake efficiency and hence engine performance. This particular phenomenon is investigated experimentally and numerically for both flight Mach numbers.

Significant steps were realized and promising results demonstrated. Work has nevertheless to be continued to increase the TRL of these technologies and take benefit of the existing test facilities and multi-physics engineering, industrial and dedicated simulation tools.

Acknowledgments

This work was performed within the '*Aerodynamic and Thermal Load Interactions with Lightweight Advanced Materials for High Speed Flight*' project investigating high-speed transport. ATLLAS, coordinated by ESA-ESTEC, is supported by the EU within the 6th Framework Programme Priority 1.4, Aeronautic and Space, Contract no.: AST5-CT-2006-030729. Further info on ATLLAS can be found on http://www.esa.int/techresources/atllas.

This consolidated overview was made possible through the inputs received from the partners involved in the project, in particular S. Soller (Astrium), M. Bouchez (MBDA), A. Passaro (Alta), M. Kuhn, J. Longo and A. Gülhan from DLR, M. Thomas and P. Duveau from Onera, M. Dalenbring (FOI), J. von Wolfersdorf (U. Stuttgart), C. Kirchberger (TUM), N. Sandham (U. Southampton), C. Wilhelmi (EADS-IW), F. Coulouvrat (UPMC) and many others in the team.

References

[1] Steelant J., 'Achievements Obtained for Sustained Hypersonic Flight within the LAPCAT project', 15th AIAA International Space Planes and Hypersonic Systems and Technologies Conference, AIAA-2008-2578, Dayton, Ohio, USA, AIAA, 28/04-01/05/2008.

[2] Recherche Aéronautique sur le Supersonique, Enjeux Scientifiques, Axes de Recherche, Structuration de la Recherche, Rapport du Comité d'Orientation Supersonique, September 2000.

[3] Commercial Viability of the High-Speed Civil Transport (HSCT), Saounatsos, Yorgos E., 1997.

[4] Ultra-Efficient Engine Technology Program, NASA-Program FY2004-2007 to develop and hand off revolutionary turbine engine propulsion technologies that will enable future generation vehicles over a wide range of flight speeds, http://www.ueet.nasa.gov/.

[5] Barbaux Y., Guedra-Degeorges D., Lapassat G., The Materials Challenge for the Future SCT, 7th European Aerospace Conference, Toulouse, France, Oct. 1994.

[6] Stephens J.R., Materials/Coatings Requirements for the HSCT Propulsion System, presentation to the Committee on Coatings for High-Temperature Structural Materials, National materials Advisory Board, National Research Council, San Antonio, Texas, Dec. 13-14, 1993.

[7] Vachal J.D., High-Speed Civil Transport Research and Technology Needs', SAE 901925, SAE Aerospace Technology Conference and Exposition, Oct. 1990, pp. 1824-1831.

[8] Darden C. M., The importance of sonic boom research in the development of future high speed aircraft', Journal of the NTA, pp. 54-62, 1992.

[9] Cain T., Zanchetta M. and Walton C.: *Aerodynamic Design of the ATLLAS Mach 3 Transport*, CEAS 2009 European Air and Space Conference, Manchester, UK, 2009.

[10] Kurzke J. and Riegler C., 'A new compressor map scaling procedure for preliminary conceptual design of gas turbines', Turbo Expo 2000, 2000-GT-0006, 2000.

[11] T. Cain, M. Zanchetta and C. Walton: *Aerodynamic Design of the ATLLAS Mach 3 Transport*, CEAS 2009 European Air and Space Conference, Manchester, UK, 2009

[12] A. Loubeau, F. Coulouvrat, "Effects of meteorological variability on sonic boom propagation from hypersonic aircraft", AIAA J., in press

[13] C. Davoine, A. Götzfried, S. Mercier, F. Popoff, A. Rafray, M. Thomas and V. Marcadon: 'Metallic hollow sphere structures manufacturing process', Material Research Society Spring meeting, San Fransisco, USA, 13-17 April 2009

[14] Marcadon V., Roques E. and Feyel F., 'Modelling of Mechanical Behaviours of Metal Hollow Sphere Regular Packing under Compression Loadings', 11th Euromech-Mecamat, Turing Italy, March 2008.

[15] J.-F. Justin: 'Investigations of High Temperature Ceramics for Sharp Leading Edges or Air Intakes of Hypersonic Vehicles', EUCASS 2009-511, European conference of Aerospace Sciences, Versailles, France, 6-9 July 2009.
[16] S. Soller, C. Kirchberger, M. Kuhn, T. Langener, M. Bouchez and J. Steelant, 'Experimental Investigation of Cooling Techniques and Materials for High-speed Flight Propulsion Systems', AIAA-2009-7374, 16th AIAA/DLR/DGLR International Space Planes and Hypersonic Systems and Technologies Conference, Bremen, Germany, October 19th – 22nd, 2009
[17] C. Kirchberger, G. Schlieben, R. Wagner, H.-P. Kau, C. Mäding, S. Soller, P. Martin, 'Design and Commissioning of a Combustion Chamber for Cooling and Material Investigations', AIAA-2009-1214, 47th AIAA Aerospace Sciences Meeting and Exhibit, Orlando, USA, 2009
[18] M. Kuhn, T. Hallberg, 'Emissivity measurements of CMC materials', Material Science and Engineering, Elsevier, planned 2010
[19] M. Kuhn, H. Hald, M. Ortelt, C. Kirchberger, G. Schlieben and H.-P. Kau, 'CMC Materials for Combustion Chamber Applications', EUCASS2009-224, 3rd European Conference for Aero-Space Sciences, Versailles, France, 05-09 July 2009.
[20] M. Kuhn, S. Hackemann, E. Klatt, 'Material characterisation of CMC materials', Material Science and Engineering, Elsevier, planned 2010
[21] C. Kirchberger, G. Schlieben, A. Hupfer, H.-P. Kau, P. Martin and S. Soller, 'Investigation on Film Cooling in a Kerosene/ GOX Combustion Chamber', AIAA-2009-5406, 45th AIAA/ASME /SAE/ASEE Joint Propulsion Conference & Exhibit, Denver, CO, USA, August 2nd-5th 2009
[22] Kirchberger C., Wagner R., Kau H.-P., Soller S., Martin P., Bouchez M. and Bonzom C., `Prediction and Analysis of Heat Transfer in Small Rocket Chambers', 46th AIAA Aerospace Sciences meeting and Exhibit, AIAA-2008-1260, Reno (NV), USA, 07-11/01 2008.
[23] Bouchez M. and Beyer S., 'PTAH-SOCAR Fuel-Cooled Composite Material Structure', 15th AIAA International Space Planes and Hypersonic Systems and Technologies Conference, AIAA-2008-2626, Dayton, Ohio, USA, AIAA, 28/04-01/05/2008.
[24] S. Soller, S. Schmidt, K. Quering, M. Bouchez, Ch. Kirchberger, 'Characterisation of convectively cooled CMC structures for high pressure combustion chamber applications', SPC2010_1839564, Space Propulsion Conference 2010, 3-6 may 2010, San Sebastian; Spain
[25] M. Bouchez, Dufour E., Cheuret F., Steelant J., Sandham N., Redford J., Roberts G., Passaro A. and Baccarella D., 'Material-Aero-Thermal Interaction Computations in the ATLLAS European Programme', 44th AIAA/ASME/SAE/ASEE Joint Propulsion Conference & Exhibit, AIAA 2008-4670, Hartford, CT, USA, July 2008.
[26] M. Bouchez, Dufour E., L. Benezich, Cheuret F., Steelant J., Gernard P., Redford J., Sandham N., Roberts G., Passaro A., Baccarella D., Dalenbring M. and Smith J., 'Material-Aero-Thermal Interaction Computations in the ATLLAS European Programme', 3rd EUCASS conference, 6-9/07/2009, Versailles, France.
[27] F. Cheuret, J. Steelant, M. Bouchez and E. Dufour, 'Performance of Existing Models for Transpiration Cooling', Space Propulsion 2008, Heraklion, Crete, May 2008.
[28] T. Langener, J. von Wolfersdorf, T. Laux and J. Steelant, 'Experimental Investigation of Transpiration Cooling with Subsonic and Supersonic Flows at Moderate Temperature Levels', 44th AIAA/ASME/SAE/ASEE Joint Propulsion Conference & Exhibit, AIAA 2008-5174, Hartford, CT, USA, July 2008.
[29] T. Langener, J. von Wolfersdorf, F. Cheuret, J. Steelant and M. Kuhn: 'Experimental And Numerical Study on Transpiration Cooling With Supersonic Flow', 19th Int. Symp. on Air Breathing Engines, ISABE, Montreal, Canada, 2009.
[30] M. Bouchez, E. Dufour, L Benezech, F. Cheuret, J. Steelant, P. Grenard, J.A. Redford, N.D. Sandham, G.T. Roberts, A. Passaro. D. Baccarella, M. Dalenbring, J. Smith and L. Cavagna: 'Multi-level Coupled Simulations of Cooled Structures in the ATLLAS European Programme', AIAA-2009-7374, 16th AIAA/DLR/DGLR International Space Planes and Hypersonic Systems and Technologies Conference, Bremen, Germany, 19-22 October, 2009
[31] F. Cheuret, J. Steelant, T. Langener and J. von Wolfersdorf, 'Simulations on Transpiration Cooling for Supersonic Flow', CEAS 2009 European Air and Space Conference, Manchester, UK, 2009.

[32] F. Cheuret and J. Steelant, 'Transpiration Cooling Modelling for Supersonic Flow', Space Propulsion 2010, San Sebastian, Spain, May 3-6, 2010.
[33] Krishnan L, Sandham N. D., 'Effect of Mach Number on the Structure of Turbulent Spots', Journal of Fluid Mechanics, Vol. 566, pp 225-234, 2006.
[34] A. Passaro, D. Baccarella, P. Caredda, J. Redford and N. Sandham, 'Experimental characterization of turbulence spots on a flat plate at Mach 6', 6th European Symposium on Aertothermodynamics for Space Vehicles, Versailles, Fance, Nov. 2008.
[35] J.A. Redford, N.D., Sandham and G.T. Roberts, 'Roughness-induced transition of compressible laminar boundary layers', Seventh IUTAM Symposium on Laminar-Turbulent Transition, KTH, Stockholm, Sweden, June 23-26, 2009.